Monthly Notices
of the
ROYAL ASTRONOMICAL SOCIETY

MNRAS **428,** 3590–3606 (2013) doi:10.1093/mnras/sts303

GRB 100219A with X-shooter – abundances in a galaxy at $z = 4.7$

C. C. Thöne,[1,2]★ J. P. U. Fynbo,[3] P. Goldoni,[4] A. de Ugarte Postigo,[1,3] S. Campana,[5] S. D. Vergani,[6] S. Covino,[5] T. Krühler,[3,7,8] L. Kaper,[9] N. Tanvir,[10] T. Zafar,[11] V. D'Elia,[12,13] J. Gorosabel,[1] J. Greiner,[7] P. Groot,[14] F. Hammer,[6] P. Jakobsson,[15] S. Klose,[16] A. J. Levan,[17] B. Milvang-Jensen,[3] A. Nicuesa Guelbenzu,[16] E. Palazzi,[18] S. Piranomonte,[12] G. Tagliaferri,[5] D. Watson,[3] K. Wiersema[10] and R. A. M. J. Wijers[9]

[1]*Instituto de Astrofísica de Andalucía, CSIC, Glorieta de la Astronomía s/n, E-8008 Granada, Spain*
[2]*Niels Bohr International Academy, Niels Bohr Institute, Blegdamsvej 17, DK-2100 Copenhagen, Denmark*
[3]*Dark Cosmology Centre, Niels Bohr Institute, University of Copenhagen, Juliane Maries Vej 30, DK-2100 København Ø, Denmark*
[4]*APC, AstroParticule et Cosmologie, Univ. Paris Diderot, CNRS/IN2P3, CEA/Irfu, Observatoire de Paris, Sorbonne Paris Cit, 10 rue Alice Domon et Leonie Duquet, F-75205 Paris Cedex 13, France*
[5]*INAF, Osservatorio Astronomico di Brera, Via E. Bianchi 46, I-23807 Merate, Italy*
[6]*GEPI, Observatoire de Paris, CNRS, Univ. Paris Diderot, 5 place Jules Janssen, F-92190 Meudon, France*
[7]*Max-Planck-Institut für extraterrestrische Physik, Giessenbachstraße, 85748 Garching, Germany*
[8]*Excellence Cluster Universe, Technische Universität München, Boltzmannstraße 2, D-85748, Garching, Germany*
[9]*Astronomical Institute Anton Pannekoek, University of Amsterdam, Science Park 904, NL-1098 XH Amsterdam, the Netherlands*
[10]*Department of Physics and Astronomy, University of Leicester, University Road, Leicester LE1 7RH*
[11]*Laboratoire d'Astrophysique de Marseille – LAM, Université Aix-Marseille & CNRS, UMR7326, 38 rue F. Joliot-Curie, F-13388 Marseille Cedex 13, France*
[12]*INAF, Osservatorio Astronomico di Roma, via di Frascati 33, I-00040 Monte Porzio Catone, Rome, Italy*
[13]*ASI-Science Data Center, via Galileo Galilei, I-00044 Frascati, Italy*
[14]*Department of Astrophysics, IMAPP, Radboud University Nijmegen, PO Box 9010, NL-6500 GL Nijmegen, the Netherlands*
[15]*Centre for Astrophysics and Cosmology, Science Institute, University of Iceland, Dunhagi 5, IS-107 Reykjavík, Iceland*
[16]*Thüringer Landessternwarte Tautenburg, Sternwarte 5, D-07778 Tautenburg, Germany*
[17]*Department of Physics, University of Warwick, Coventry, CV4 7AL*
[18]*INAF, IASF di Bologna, via Gobetti 101, I-40129 Bologna, Italy*

Accepted 2012 October 28. Received 2012 October 9; in original form 2012 August 13

ABSTRACT

Abundances of galaxies at redshifts $z > 4$ are difficult to obtain from damped Lyα (DLA) systems in the sightlines of quasars (QSOs) due to the Lyα forest blanketing and the low number of high-redshift QSOs known to date. Gamma-ray bursts (GRBs) with their higher luminosity are well suited to study galaxies out to the formation of the first stars at $z > 10$. The large wavelength coverage of the X-shooter spectrograph makes it an excellent tool to study the interstellar medium of high-redshift galaxies, in particular if the redshift is not known beforehand. In this paper, we determine the properties of a GRB host at $z = 4.667\,23$ from absorption lines combined with X-ray and optical imaging data. This is one of the highest redshifts where a detailed analysis with medium-resolution data is possible. We measure a relatively high metallicity of $[\mathrm{S/H}] = -1.1 \pm 0.2$ for a galaxy at this redshift. Assuming ultraviolet pumping as origin for the fine-structure lines, the material observed is between 0.3 and 1.0 kpc from the GRB. The extinction determined by the spectral slope from X-rays to the infrared shows a moderate value of $A_V = 0.13 \pm 0.05$ mag and relative abundances point to a warm disc extinction pattern. Low- and high-ionization as well as fine-structure lines show a complicated kinematic structure probably pointing to a merger in progress. We also detect one intervening system at $z = 2.18$. GRB-DLAs have a shallower evolution of metallicity with redshift than QSO absorbers and no evolution in their H I column density or ionization fraction.

★ E-mail: cthoene@iaa.es

GRB hosts at high redshifts seem to continue the trend of the metallicity–luminosity relation towards lower metallicities but the sample is still too small to draw a definite conclusion. While the detection of GRBs at $z > 4$ with current satellites is still difficult, they are very important for our understanding of the early epochs of star and galaxy formation.

Key words: galaxies: abundances – galaxies: high-redshift – galaxies: ISM – gamma-ray burst: individual: GRB 100219A.

1 INTRODUCTION

Determining the properties of the interstellar medium (ISM) in high-redshift galaxies is difficult due to their extreme faintness. Detailed and resolved studies using emission lines in the optical/near-infrared (NIR) range are restricted to redshifts up to $z \sim 3$ with current facilities (see, e.g., Maiolino et al. 2008; Förster-Schreiber et al. 2009) and only with the help of gravitational lensing beyond this redshift [see, e.g., Swinbank et al. (2009) for resolved studies of a gravitationally lensed galaxy at $z = 4.9$]. The use of gamma-ray bursts (GRBs) as lighthouses is a promising way to study the properties of galaxies at $z > 4$, similar to what has been done since many years with intervening absorption systems towards quasars (QSOs). In contrast to QSOs, GRBs with their higher luminosities can probe more central and denser regions of those galaxies. Long GRBs are connected to massive star formation [SF; see, e.g., Woosley & Bloom 2006 for a review of the GRB–supernova (SN) connection]; hence, GRBs probe star-forming places across cosmic history (e.g. Fruchter et al. 2006).

GRB afterglows constitute a powerful source for absorption-line studies as they have smooth, featureless intrinsic spectra on which the intervening ISM in the host imprints absorption lines from different metals. Optical spectroscopy allows the determination of metallicities from $z \sim 1.7$ to $\sim$6 when those metal absorption lines get redshifted into the NIR. X-shooter at the European Southern Observatory (ESO) Very Large Telescope (VLT; D'Odorico et al. 2006; Vernet et al. 2011) with its wavelength coverage from 3000 to 24 800 Å facilitates detailed investigations of galaxies up to redshifts of $z \sim 11-13$, provided GRBs exist at such high redshifts. The broad wavelength coverage of X-shooter also allows us to fit an extinction curve and to derive the reddening from the shape of the continuum, assuming an intrinsic power law for the continuum. In most cases, its medium resolution allows the fitting of the absorption lines with Voigt profiles providing a more accurate determination of the column density compared to low-resolution methods.

Previous studies have revealed a diverse picture of GRB host metallicities but they suffer from a small sample size, with currently about 20 metallicities published in the literature (for the largest samples see, e.g., Fynbo et al. 2006; Prochaska et al. 2007; Savaglio, Glazebrook & LeBorgne 2009). Metallicities of GRB hosts seem to be on average higher than those obtained from QSO damped Lyα systems (DLAs), in particular at higher redshifts (e.g. Fynbo et al. 2006). GRB host metallicities also seem to show a slower evolution with redshift, albeit with a large scatter at any given redshift. Both GRB and QSO samples, however, show subsolar metallicities, in some cases down to 1/100 solar or less (e.g. GRB 050730, D'Elia et al. 2007; GRB 090926A, Rau et al. 2010; D'Elia et al. 2010). The difference between the two samples can be explained by QSO absorbers probing the outer, less metal-rich regions of galaxies due to their lower luminosity and the sightlines being selected according to the cross-section, and by GRB hosts being larger than QSO-DLA galaxies (Fynbo et al. 2008).

The gas observed in GRB absorption-line studies is mostly in a low ionization state (see, e.g., Fynbo et al. 2009) which makes it a good representation of the cold gas in the host galaxy, mostly unaffected by the GRB itself. The same is the case for the material observed in QSO absorbers; however, one has to consider that QSOs and GRB-DLAs are likely probing different regions in the galaxy. Exceptions of highly ionized material in GRB afterglow spectra might point to a special environment of material from the vicinity of the GRB itself (e.g. GRB 090426, Thöne et al. 2011) and hence are not representative for the metallicity of GRB hosts in general.

Extinction in GRB hosts is usually low, although somewhat higher than that in QSO-DLAs. For a sample of 41 *Swift* GRB afterglow spectra, Zafar et al. (2011) found that 90 per cent have $A_V < 0.65$ mag with an average of 0.24 mag and a Small Magellanic Cloud (SMC) extinction law. A similar result was found from photometric data of *Swift* GRBs by Kann et al. (2010). However, high extinction makes the detection of the afterglow at optical wavelengths difficult and hence this result is somewhat biased (e.g. Greiner et al. 2011; Krühler et al. 2011b). The extinction in GRB hosts also seems to decrease with redshift (Kann et al. 2010; Zafar et al. 2011). Again, we might miss more highly extinguished high-redshift bursts, due to the shape of the extinction curve which particularly affects optical observations, as these probe the rest-frame ultraviolet (UV) at those redshifts. Furthermore, dust is produced by asymptotic giant branch stars and SNe which, in a young star-forming region at high redshifts, might not be present or not have produced enough dust yet (see e.g. Gall, Hjorth & Andersen 2011).

GRB 100219A was discovered in an image trigger by the *Swift* satellite (Gehrels et al. 2004) on 2010 February 19, 15:15:46 UT (Rowlinson et al. 2010) and had a duration of $T_{90} = 18.8 \pm 5.0$ s (Baumgartner et al. 2010). An X-ray as well as an optical afterglow (Jakobsson et al. 2010) was found. A nearby galaxy detected in the Sloan Digital Sky Survey (SDSS) was first assumed to be the host galaxy (Bloom & Nugent 2011), implying a low redshift for this GRB. However, Gamma-Ray Burst Optical/Near-Infrared Detector (GROND) reported a g'-band dropout and suggested a redshift of $z \sim 4.5$ (Krühler et al. 2010). We took spectra with the second-generation instrument X-shooter at the VLT, revealing a DLA system and a number of absorption lines at a common redshift of $z = 4.6667$ (de Ugarte Postigo et al. 2010a; Groot et al. 2010). This redshift was later confirmed by GMOS-N/Gemini-N (Cenko et al. 2010a).

In the following, we present the observations and data reduction of the X-shooter spectra (Section 2), the analysis of the absorption lines in the host as well as the metallicities and abundances derived from fitting the column densities of the absorption lines (Section 3), a broad-band fit to the spectral energy distribution (SED) from X-ray to NIR (Section 4) and a description of the intervening system at $z = 2.18$ (Section 5). Finally, we place the metallicity of GRB 100219A in the context of other GRB host metallicities and high-redshift galaxies in general (Section 6). For all calculations we use a cosmology with $\Omega_M = 0.27$, $\Omega_\Lambda = 0.73$ and $H_0 = 71$ km s^{-1} Mpc^{-1}. The flux of a GRB is defined to behave as $F_\nu \propto t^{-\alpha}\nu^{-\beta}$.

2 OBSERVATIONS

2.1 X-shooter spectroscopy

We observed the afterglow of GRB 100219A starting on 2010 February 20, 02:31 UT (12.5 h after the trigger) with X-shooter at the VLT under good seeing conditions (∼0.7 arcsec). The observations consisted of four different exposures with an exposure time of 1200 s each. The individual exposures were taken by nodding along the slit with an offset of 2 arcsec between exposures, using a standard ABBA sequence.[1] The spectra cover the wavelength range from ∼3000 to 25 000 Å at a resolution of $R \sim 5300$–8800 [the visible (VIS)/NIR range] and an average signal-to-noise ratio (S/N) of ∼4 pixel^{-1}. Due to the high redshift and the faintness of the source, we detect a continuum from the afterglow in the range from ∼5100 (Lyman break) to 23 000 Å.

The spectra were processed with version 1.3.7 of the X-shooter data reduction pipeline (Goldoni et al. 2006; Modigliani et al. 2010). The pipeline transforms the detected counts in physical quantities while propagating the errors and bad pixels consistently during the process. The reduction consists of the following steps. First, the raw frames are subtracted from each other and cosmic ray hits are detected and corrected using the method developed by van Dokkum (2001). The frames were then divided by a master flat-field produced using daytime flat-field exposures with halogen lamps. From the flat-fielded raw frames, the orders are extracted and rectified in wavelength space using a wavelength solution previously obtained from calibration frames. The resulting rectified orders are then shifted by the offset used in the observation and merged to obtain the final 2D spectrum, in overlapping regions the orders are weighted by the errors.

From the resulting merged 2D spectrum we extracted a 1D spectrum together with a corresponding error spectrum and a bad pixel map using a simple point spread function (PSF) weighting scheme under IDL. The error spectrum was derived from the noise of the raw frames propagated through all the reduction steps using the standard formulae of error propagation. However, probably due to the presence of the nearby galaxy, the absolute flux level of the 1D spectrum was too low. Indeed, in the UVB arm and in the strong atmospheric absorption bands in the NIR arm, the median flux goes below zero by an amount slightly greater than the 1σ error which is unphysical. We therefore applied the same positive offset to the flux in the three arms to correct for this effect and put the median flux to zero in those regions.

For the flux calibration we extracted a spectrum from an observation of the flux standard GD71 (Bohlin, Colina & Finley 1995) in staring mode. The reduction procedure is the same as for the science object, with the exception that the sky emission lines are subtracted according to the Kelson (2003) method. The standard-star spectrum was then divided by the flux table of the same star obtained from the CALSPEC *Hubble Space Telescope* data base[2] to produce the response function. After division by the flux table, we verified that the shape of the response function was compatible with the ones found in previous reductions by our group. The response was then interpolated in the atmospheric absorption bands in VIS and NIR and applied to the spectrum of the source. No telluric correction was performed. The final spectrum was transformed from air to vacuum wavelengths. An image of the field including the slit position and a part of the 2D spectrum is shown in Fig. 1.

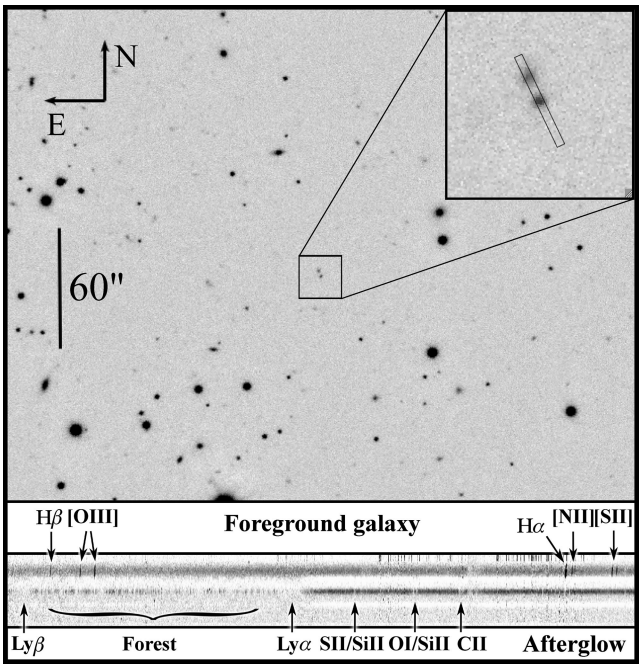

Figure 1. Field of GRB 100219A in the z band from WHT/ACAM at 8.8 h after the burst. The slit position across the afterglow and the nearby galaxy is indicated. The lower panel shows the 2D spectrum with the spectrum of the afterglow (lower trace) and the unrelated galaxy in the slit (upper trace) with some emission lines indicated.

2.2 Imaging observations

The GROND (Greiner et al. 2008) mounted at the Max Planck Gesellschaft/ESO 2.2 m telescope at La Silla observatory in Chile observed the field of GRB 100219A starting on 2010 February 20, 00:30 UTC, 9.24 h after the Burst Alert Telescope (BAT) trigger (Krühler et al. 2010). Further imaging was performed on three later epochs with mean times of 36.6, 61.5 and 110.7 h after T_0. In addition, we obtained two epochs of NIR observations in the JHK_s filters with HAWK-I/VLT (Kissler-Pattig et al. 2008) at mean times of 59.6 and 107.8 h after the trigger, respectively. We also obtained a single-epoch observation of the field using the auxiliary port camera (ACAM) on the 4.2 m William Herschel Telescope (WHT) on La Palma, starting 8.8 h post-burst. We used the z-band filter, with a total exposure of 1800 s.

All photometric data were reduced in a standard manner using PYRAF/IRAF, similar to the procedure outlined in Krühler et al. (2008). Given the presence of a bright foreground galaxy 3 arcsec from the afterglow, PSF fitting photometry was used for the photometry in all epochs. The stacked images were flux calibrated against GROND observations of SDSS fields (Abazaijan et al. 2009) taken immediately before or after the field of GRB 100219A for the optical $g'r'i'z'$, and magnitudes of 2MASS field stars (Skrutskie et al. 2006) for the JHK_s filters. All data were corrected for the Galactic foreground extinction of $E(B-V) = 0.076$ according to Schlegel, Finkbeiner & Davis (1998) assuming a total-to-selective extinction of $R_V = 3.08$. The WHT observations were calibrated via the GROND magnitudes for stars in the field. For a log of the observations and photometry see Table 1, the light curve is shown in Fig. 2.

[1] The spectrum is taken at position A in the slit, then shifted along the slit to position B, etc.

[2] Bohlin (2007), http://www.stsci.edu/hst/observatory/cdbs/calspec.html

Table 1a. Late-time optical photometry. Times are mid-times of the observations compared to the burst trigger time. Observations in parentheses are the stack of the three preceding images. Magnitudes are given in the AB system and corrected for Galactic foreground extinction of $E(B-V) = 0.076$. Upper limits are 3σ.

Date (h)	Exp. time (s)	Instrument	g' (AB mag)	r' (AB mag)	i' (AB mag)	z' (AB mag)
8.812	1800	WHT/ACAM	–	–	–	21.14±0.017
9.516 39	460	GROND	–	22.55 ± 0.15	21.26 ± 0.09	21.06 ± 0.11
9.733 61	460	GROND	–	22.75 ± 0.17	21.29 ± 0.07	20.99 ± 0.10
10.9039	1460	GROND	–	22.88 ± 0.05	21.51 ± 0.05	21.32 ± 0.06
11.4039	1460	GROND	–	22.88 ± 0.06	21.55 ± 0.04	21.42 ± 0.05
11.9033	1460	GROND	–	22.99 ± 0.06	21.64 ± 0.04	21.44 ± 0.07
(11.4036	4380	GROND	25.65 ± 0.37	22.96 ± 0.04	21.54 ± 0.03	21.34 ± 0.04)
36.5767	4380	GROND	>25.65	24.48 ± 0.14	23.28 ± 0.11	23.39 ± 0.17
61.4692	4380	GROND	>25.64	24.99 ± 0.20	23.60 ± 0.15	23.65 ± 0.18
110.692	4380	GROND	>25.39	25.40 ± 0.41	24.75 ± 0.42	23.95 ± 0.32
685 d	1440	OSIRIS/GTC	–	–	26.7 ± 0.5	–

Table 1b. NIR photometry. Times are mid-times of the observations compared to the burst trigger time. Observations in parentheses are the stack of the three preceding images. Magnitudes are given in the AB system and corrected for Galactic foreground extinction of $E(B-V) = 0.076$. Upper limits are 3σ.

			J (AB mag)	H (AB mag)	K_s (AB mag)
10.9106	1200	GROND	20.78 ± 0.17	20.24 ± 0.16	–
11.4106	1200	GROND	20.99 ± 0.20	20.32 ± 0.16	–
11.9097	1200	GROND	20.75 ± 0.16	20.65 ± 0.25	–
(11.4100	3600	GROND	20.84 ± 0.12	20.43 ± 0.12	20.24 ± 0.26)
36.5831	3600	GROND	>22.22	–	–
59.5956	2280	HAWK-I	23.79 ± 0.47	>22.84	22.5 ± 0.23
107.760	4560	HAWK-I	24.08 ± 0.34	23.79 ± 0.27	23.06 ± 0.24

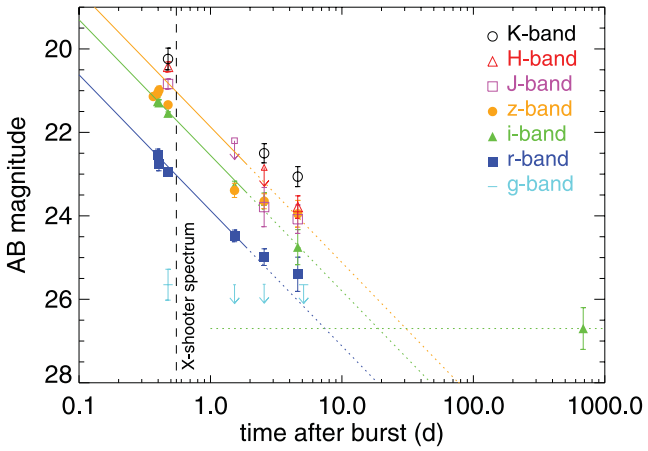

Figure 2. Multicolour light curve of the late optical observations from GROND, HAWK-I and ACAM, the last g-band limit is offset for clarity. The solid/dashed lines are the decay slope of $\alpha = -1.31$ as derived from a common fit to the r', i' and z' bands at the first four epochs. The following two epochs were excluded as there might be some rebrightening of the afterglow. The last point is the detection of the host galaxy. Magnitudes are in the AB system and corrected for Galactic extinction (see the values in Table 1).

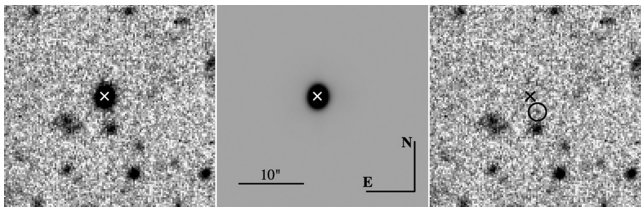

Figure 3. Observations of the host galaxy candidate of GRB 100219A with OSIRIS/GTC, i' band. Left-hand panel: combined i'-band observations. Middle panel: model of the foreground galaxy, the centre is indicated by a cross. Right-hand panel: image with the residuals after subtracting the galaxy model. A faint object is visible with $i' = 26.7 \pm 0.5$ (circle). The host candidate is at a distance of 0.4 ± 0.3 arcsec from the afterglow position, corresponding to a physical distance of 2.6 ± 2.0 kpc. The value is consistent with what has been found for other GRB afterglows (Bloom, Kulkarni & Djorgovski 2002; de Ugarte Postigo et al. 2012).

Fitting the afterglow light curve with all available optical/NIR data simultaneously with an achromatic power law results in a temporal index of $\alpha = 1.31^{+0.03}_{-0.04}$ with a χ^2 of 36 for 30 degrees of freedom (d.o.f.). There is a trend of flattening or rebrightening observed at late times ($t > 50$ h) and we therefore exclude the last two epochs from the fit. Mao et al. (2012) also found late achromatic bumps in the optical/X-ray light curve during the first day.

To determine whether the late afterglow epochs might be dominated by a (bright) underlying host galaxy, we reobserved the field on 2011 December 27 in the i' band with OSIRIS/Gran Telescopio Canarias and a total exposure time of 12 × 120 s. Since the GRB position lies near the bright foreground galaxy at $z = 0.25$ also present in the X-shooter spectrum (see above), we use GALFIT (Peng et al. 2002) to subtract the contribution of this foreground galaxy. The subtraction with a Sérsic profile works very well as shown in Fig. 3 and we detect a weak object at the position of the GRB with

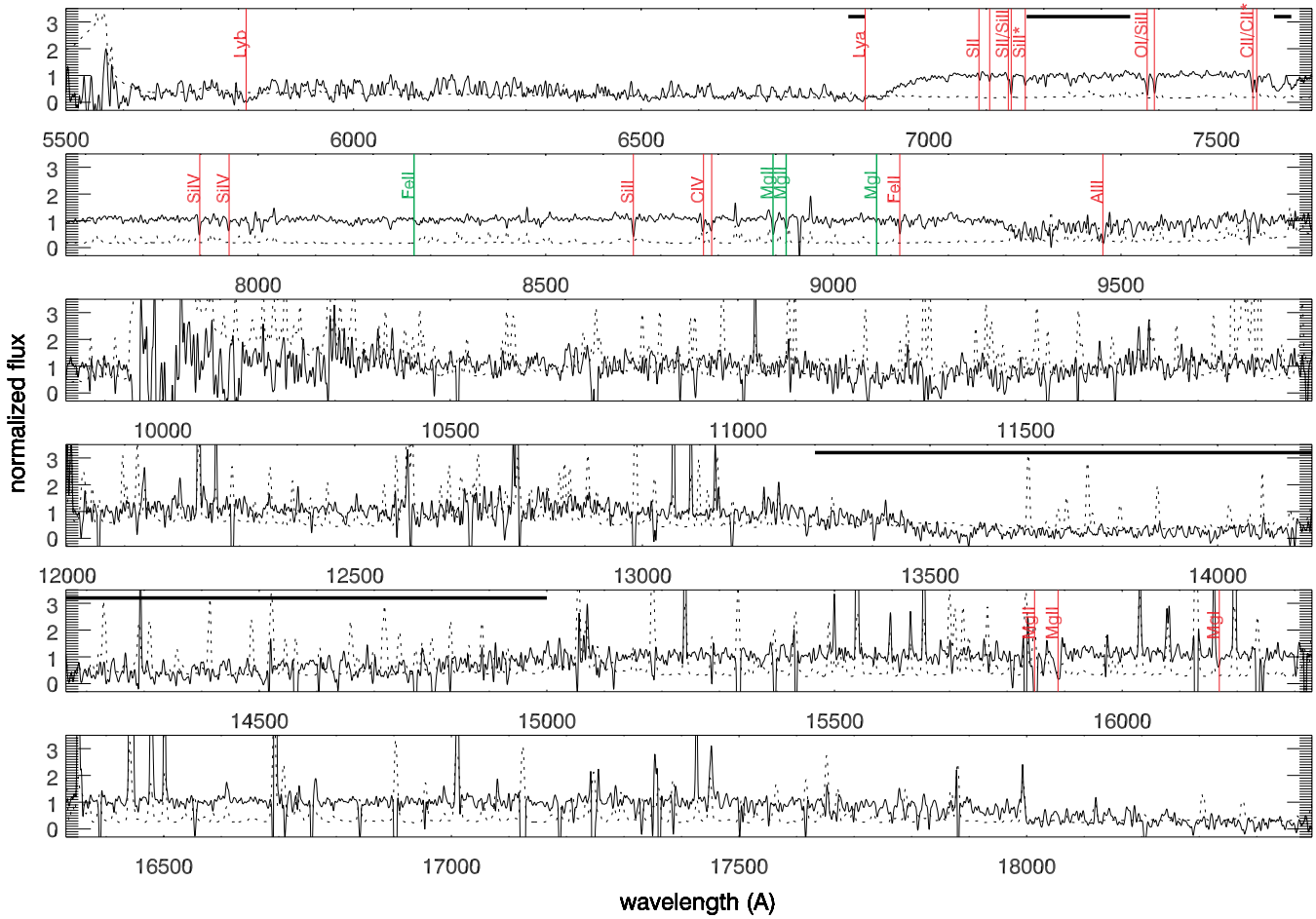

Figure 4. X-shooter spectrum of 100219A with the detected absorption lines from the host system (red) and the intervening system (green) indicated. The horizontal black bars denote the atmospheric absorption bands, the dotted line shows the error spectrum. The UVB arm is not shown since it is below the Lyman limit. The spectrum above ∼18 000 Å is not plotted due to low S/N and the absence of detected lines.

$i' = 26.7 \pm 0.5$ (2σ, AB magnitudes), using the same reference stars as for the afterglow photometry. The host galaxy candidate can therefore not have contributed significantly at 2–3 d post-burst and the deviation from the power-law decay of the afterglow might be due to a late rebrightening.

3 ABSORPTION LINES IN THE GRB SYSTEM

We detect a number of resonant absorption lines from the GRB host galaxy, including a DLA, as well as one intervening system (see Fig. 4). The strongest absorption lines from the host system show at least five velocity components spanning a range of ∼200 km s^{-1}. We also detect two fine-structure transitions of Si II and one from C II, as have also been detected in a number of other GRB spectra (first detected by Vreeswijk et al. 2004). These transitions are likely produced by UV pumping of the excited levels by the radiation from the GRB itself. However, Si II* has also been observed in star-forming galaxies where they could be produced by UV radiation from young stars (see e.g. Christensen et al. 2011). Fine-structure lines that were so far only found in GRB environments such as Ni II* or Fe II* are not detected in our spectrum (Vreeswijk et al. 2007; Christensen et al. 2011).

3.1 Line fitting and properties

From the absorption lines detected in the X-shooter spectrum, de Ugarte Postigo et al. (2010a) had determined a redshift of $z = 4.6667 \pm 0.0005$, which we refine in the following. We downgrade the spectrum to a resolution of ∼2 Å to eliminate the velocity structure and fit Gaussians to all well-detected absorption lines. We do not include the high-ionization lines such as Si IV and C IV as well as the fine-structure lines since those have a different velocity structure (see also Section 3.3). This gives us the redshift of the gas with the strongest absorption component, which coincides with the redshift of the main absorption component of S II, the weakest absorption line detected. Wavelengths have been corrected for the heliocentric velocity shift of 5.26 km s^{-1} at the time of our spectrum. The final redshift is $z = 4.667\,23 \pm 0.000\,37$, which we adopt as systemic redshift (defined as $v = 0$ km s^{-1} in the following).

The equivalent widths (EWs) are also determined from the Gaussians fitted to the lines in the smoothed spectrum. The errors on the EWs are based on the noise spectrum in the 95 per cent width interval of the fitted Gaussian. Errors from the Gaussian fit itself are not included. In Table 2 we list the detected lines with their corresponding wavelengths and EWs, values are given in rest frame.

From the full-resolution spectrum we determine the column densities by fitting Voigt profiles to the different absorption components using the FITLYMAN context in MIDAS.[3] This program fits Voigt profiles with the atomic parameters for each transition by convolving them with the resolution of the instrument. If the resolution is high

[3] http://www.eso.org/sci/software/esomidas/

Table 2. Absorption-line list for the GRB and the intervening system. All wavelengths are in vacuum, EWs are given in rest frame. The Mg II lines of the GRB host system are severely affected by atmospheric lines; hence, we cannot give exact values.

Line	λ_{rest} (Å)	λ_{obs} (Å)	EW (Å)	log N (cm^{-2})
GRB				
Lyα	1215.670	6894	–	21.14 ± 0.15
S II	1250.584	7090.375	0.12 ± 0.04	15.25 ± 0.15
S II	1253.811	7107.643	0.14 ± 0.04	15.25 ± 0.15
S II	1259.519	7139.867	0.10 ± 0.04	15.25 ± 0.15
Si II	1260.422	7145.059	0.52 ± 0.04	15.15 ± 0.25
Si II*	1264.738	7170.786	0.47 ± 0.05	13.60 ± 0.15
O I	1302.169	7381.448	0.67 ± 0.04	16.90 ± 0.46
Si II	1304.370	7394.606	0.55 ± 0.05	15.15 ± 0.25
C II	1334.532	7564.966	0.56 ± 0.05	15.18 ± 0.26
C II*	1335.663	7571.421	0.45 ± 0.05	15.20 ± 0.30
Si IV	1393.755	7900.031	0.40 ± 0.05	14.13 ± 0.16
Si IV	1402.770	7950.811	0.34 ± 0.05	14.13 ± 0.16
Si II	1526.708	8654.931	0.50 ± 0.07	15.15 ± 0.25
C IV	1548.195	8775.541	0.38 ± 0.08	14.45 ± 0.10
C IV	1550.770	8789.557	0.41 ± 0.04	14.45 ± 0.10
Fe II	1608.451	9118.284	0.33 ± 0.04	14.73 ± 0.11
Al II	1670.787	9471.844	0.79 ± 0.07	14.00 ± 0.25
Mg II	2796.352	(15852.8)	–	(>13.72)
Mg II	2803.530	15893.554	∼1.4	>13.72
Mg I	2852.965	16167.345	0.45 ± 0.08	12.99 ± 0.22
Intervening system				
Fe II	2600.173	8270.620	0.10 ± 0.04	13.13 ± 0.12
Mg II	2796.352	8895.826	0.90 ± 0.08	13.69 ± 0.08
Mg II	2803.530	8918.049	0.50 ± 0.10	13.69 ± 0.08
Mg I	2852.965	9074.719	0.10 ± 0.05	12.07 ± 0.14

enough, this program obtains wavelengths of the individual components, column density and *b*-parameter (turbulent and thermal) by fitting the absorption profile. Since our resolution is not good enough to determine all the parameters from single absorption lines, we have to make some assumptions: thermal broadening is not expected and we assume the same turbulent *b*-parameter for the same velocity components in all ions where the component appears.

Due to the low S/N, limited resolution and blending of different components, we obtained the turbulent *b*-parameter of the resonant lines from fitting one wing of the different components in the element that, in each specific component, showed the least blending and/or saturation. The resulting *b*-parameters are: 11.2, 9.5, 10.2 and 6.5 km s^{-1} for components I, II, III and V, respectively, and 6, 10, 10 and 5 km s^{-1} for the high-ionization lines. For components 0 and IV we take the average *b*-parameter of 12.6 km s^{-1} (see de Ugarte Postigo et al. 2012) resulting from a sample of high-resolution GRB spectra. *b*-parameters for Mg as well as the intervening system could be obtained directly from FITLYMAN.

The column density of hydrogen was obtained from fitting the red wing of the Lyα line (see Fig. 5). Lyβ is also in the range of the spectrum but cannot be fitted since it is embedded in the Lyα forest and the Lyα forest blanketing is already playing a role at $z = 4.7$. For Mg II, we can only fit the λ2803Å line of the doublet since the λ2796Å line is heavily contaminated by atmospheric lines and even for Mg II λ2803Å we are only able to give fits for the three bluemost components. This is one of the highest redshift GRB hosts for which Mg II has been detected. At similar redshifts, strong Mg II absorbers (EW > 1 Å) have been detected in QSO sightlines (e.g. Jiang et al. 2007).

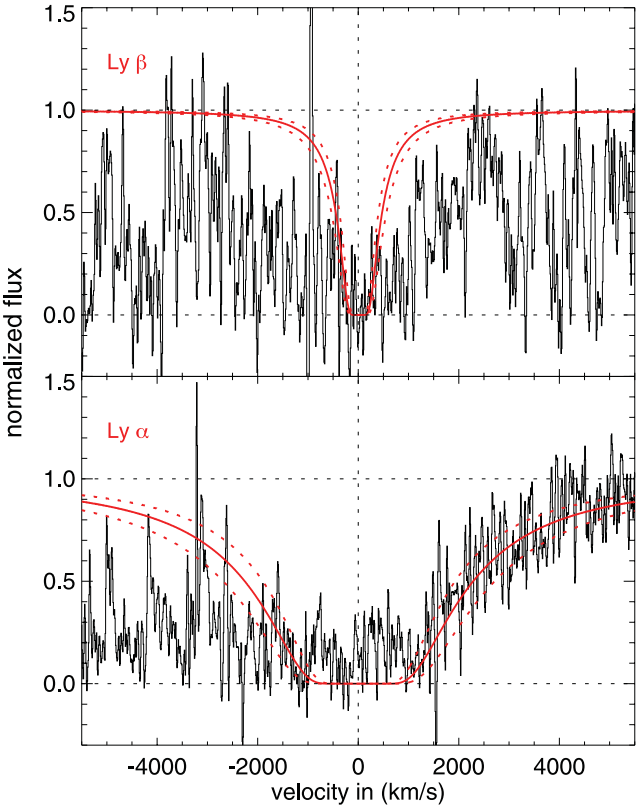

Figure 5. Lyα and Lyβ absorption at the redshift of the GRB host. Lyβ was not fitted due to the Lyα forest, the fit shows the Lyβ Voigt profile with the parameters adopted from the fit to Lyα.

In Table 3 we present the velocities and column densities for the different components. Figs 6 and 7 show the Voigt profile fits to one transition from each ion, selected to either have the best S/N or being the least saturated transition or the one least affected by skylines and/or blending with other lines. The components are not at the same velocities for all lines which will be discussed in Section 3.3.

3.2 Metallicity

The total column densities of different absorption lines allow us to determine the metallicity of the galaxy hosting GRB 100219A. Leaving out Al and Mg which are affected by atmospheric lines we obtain the following metallicities: $[C/H] = -2.0 \pm 0.2$, $[O/H] = -0.9 \pm 0.5$, $[Si/H] = -1.4 \pm 0.3$, $[S/H] = -1.1 \pm 0.2$ and $[Fe/H] = -1.9 \pm 0.2$. For C and Si we added the contribution of the low- and high-ionization resonant and fine-structure transitions. All values are compared to the solar abundances from Asplund et al. (2009).

O and S are the elements known to be least affected by dust depletion but O I is usually saturated and the column density might not be fully reliable. However, for our spectrum they both show similar metallicities. Jenkins (2009) investigated the depletion for a range of different elements in sightlines through the Milky Way (MW). With this, he developed a method to determine the degree of depletion $F*$ and the metallicity by a linear fit of abundances in case of depletion. The normalization of this fit then gives a synthetic hydrogen abundance, whose difference to the measured H I column density (if available) gives the metallicity. Applying this method for our spectra results in a mild depletion ($F* = 0.12$), leaving

Table 3. Column densities for the five velocity components in the absorption lines as shown in Figs 6 and 7. Transitions in parentheses are detected but affected by skylines or blended and have not been used to fit the column densities.

Ion, transition (Å)	**0**		**I**		**II**		**III**		**IV**		**V**	
	Δv (km s^{-1})	log N (cm^{-2})	Δv (km s^{-1})	log N (cm^{-2})	Δv (km s^{-1})	log N (cm^{-2})	Δv (km s^{-1})	log N (cm^{-2})	Δv (km s^{-1})	log N (cm^{-2})	Δv (km s^{-1})	log N (cm^{-2})
S II 1250/53/59	–	–	**+35**	14.42 ± 0.24	**0**	15.16 ± 0.18	–	–	–	–		
C II 1334	–	–	**+35**	14.99 ± 0.37	**0**	13.78 ± 0.26	**−28**	14.24 ± 0.28	**−67**	13.60 ± 0.21	**−95**	13.87 ± 0.36
C II* 1335.6/35.7	–	–	**+35**	13.62 ± 0.21	**0**	14.81 ± 0.53	**−28**	14.76 ± 0.27	**−67**	13.62 ± 0.18	–	–
C IV 1548, 1550	–	–	–	–	**+15**	13.49 ± 0.19	**−18**	13.92 ± 0.17	**−45**	13.58 ± 0.13	**−100**	14.07 ± 0.19
Si II 1304 (1260, 1526)	**+75**	13.79 ± 0.33	**+45**	14.44 ± 0.48	**+18**	14.59 ± 0.45	**−13**	14.41 ± 0.35	**−38**	13.91 ± 0.18	–	–
Si II* 1264	–	–	**+45**	12.38 ± 0.32	**+18**	13.22 ± 0.26	–	–	**−38**	13.25 ± 0.19	–	–
Si IV 1393, 1402	–	–	–	–	**+15**	12.53 ± 0.42	**−18**	13.62 ± 0.34	**−45**	13.68 ± 0.18	**−100**	13.44 ± 0.23
Fe II 1608 (2344)	–	–	**+45**	14.11 ± 0.15	**+18**	14.25 ± 0.22	**−13**	14.20 ± 0.20	**−38**	13.55 ± 0.27	–	–
O I 1302	–	–	**+45**	15.93 ± 0.43	**0**	14.67 ± 0.43	**−28**	16.76 ± 0.56	–	–	**−95**	14.18 ± 0.25
Al II 1670	**+75**	12.65 ± 0.19	**+45**	13.21 ± 0.39	**+7**	13.32 ± 0.48	**−13**	13.00 ± 0.65	**−38**	12.96 ± 0.26	**−95**	12.88 ± 0.36
Mg I 2852	–	–	**+55**	11.47 ± 0.49	**+16**	12.24 ± 0.36	**−13**	12.35 ± 0.34	**−43**	12.54 ± 0.38	–	–
Mg II 2803 (2796)	(**+60**	14.99 ± 0.79)	–	–	(**+6**	14.74 ± 0.70)	**−45**	13.38 ± 0.14	**−77**	13.28 ± 0.63	**−111**	12.94 ± 0.17

Bold values are velocities

out the low abundance from C, a depletion pattern similar to a warm disc+halo in the MW (see also Savage & Sembach 1996) and a metallicity of around −1.04. The relatively large error in the depletion of 0.47 would also allow for other warm ISM models, but still rules out a cold disc abundance pattern. In Fig. 8 we plot the values from GRB 100219A according to the method of Jenkins (2009) together with the depletion factors of different patterns from our MW as defined in Savage & Sembach (1996).

Throughout the paper, we will refer to the metallicity derived from sulphur [S/H] $= -1.1 \pm 0.2$ or $\sim 1/10$ Z$_\odot$ since it is known to be one of the elements least affected by dust depletion. This metallicity lies well within the value found for other GRB hosts at lower redshifts (see Table 4 and Fig. 9). In fact, GRB host metallicities in the range $3 < z < 4$ show a large scatter between $<1/100$ Z$_\odot$ (GRB 050730, D'Elia et al. 2007) and >0.3 Z$_\odot$ (GRB 090205, D'Avanzo et al. 2010, which has only a slightly lower redshift than GRB 100219A). QSO-DLA metallicities at this redshift range are considerably lower with a mean metallicity of around 1/100 Z$_\odot$. Measurements from QSO absorption systems at $z = 5$ and 6 (Becker et al. 2011) indicate an even lower metallicity for those galaxies. We will discuss this further in Section 5.2.

3.3 Kinematics

The strongest absorption lines cover a velocity range of around 150 km s^{-1}, but with different components and distributions. C II, O I and Al II show the largest velocity spread while Si II and Fe II are narrower and have a somewhat different distribution. Mg II has a completely different velocity distribution and might trace different material than the other resonant lines.

While for GRBs high- and low-ionization lines often show the same velocity range, the opposite is true for QSO absorbers where high- and low-ionization lines trace different volumes (ionized halo gas versus low-ionization gas in the central parts of the galaxy). The situation is different for GRB 100219A. The high-ionization lines of Si IV and C IV are blueshifted compared to their low-ionization counterparts but have a similar distribution of components. The mean absorption of the high-ionization lines is at $v = -50$ km s^{-1} while it is at $v = 0$ km s^{-1} (by definition) for the low-ionization lines. This also implies a different ionization of the material in the individual velocity components with a very low ionization for components I and II, the strongest components of the low-ionization lines, provided the absorption actually arises in the same place for low- and high-ionization lines.

The situation is equally puzzling comparing the fine-structure lines. The fine-structure lines of Si II* and C II* show a similar velocity width than the resonant counterparts but the strongest absorption component of the fine-structure line does not coincide with the main absorption (or the redmost) component and lies at around −40 km s^{-1}. Provided that the fine-structure lines originate from the UV radiation of the GRB, the strongest fine-structure absorption should be closest to the GRB site and is therefore often found to be in the redmost component (see, e.g., Thöne et al. 2008), as expected from an ordered velocity field in the host galaxy. If the GRB radiation is indeed responsible for the excitation of our fine-structure lines, component III must be the one closest to the GRB as we will show in the following.

Using the ratio between fine-structure and resonant abundances of the same element, one can determine a rough distance of the material from the GRB itself, assuming that the levels are populated by indirect UV pumping from the GRB (see Prochaska, Chen & Bloom 2006; Vreeswijk et al. 2007). We compute the distance between the GRB and the absorbing systems using a time-dependent, photoexcitation code (see D'Elia et al. 2007; Vreeswijk et al. 2007 for details) predicting the ratio between fine-structure and ground-state levels. We use as input the GRB flux, spectral and temporal indices estimated in this paper, a Doppler parameter of 12.6 km s^{-1} (see Section 3.1), and we assume that the gas is completely in its ground state when the GRB explodes. The output of our code is then compared to the Si II column densities for the components that also show absorption from Si II*, i.e. components I, II and III. The initial Si II ground-state column densities are obtained by summing the contribution from Si II and Si II* for each component. Given the large error bars of our data, we only derive an order of magnitude for the GRB-absorber distances. We find that component IV is the closest to the GRB, at a distance of $d_{\rm IV} \sim 300$ pc and a similar distance for component II while component I is at $d_{\rm I} \sim 1$ kpc.

The complicated velocity structure of the different absorption species could be an indication for a chaotic velocity field in this galaxy. High-redshift star-forming galaxies are likely nothing close to the ordered, rotation-supported galaxies we see today. Integral field unit (IFU) observations of galaxies at $z \sim 2$ and 3 show a high velocity dispersion of the measured emission lines (see, e.g., Law et al. 2009, and references therein) whose origin is still highly debated. Among other mechanisms, mergers (Puech et al. 2006, 2007)

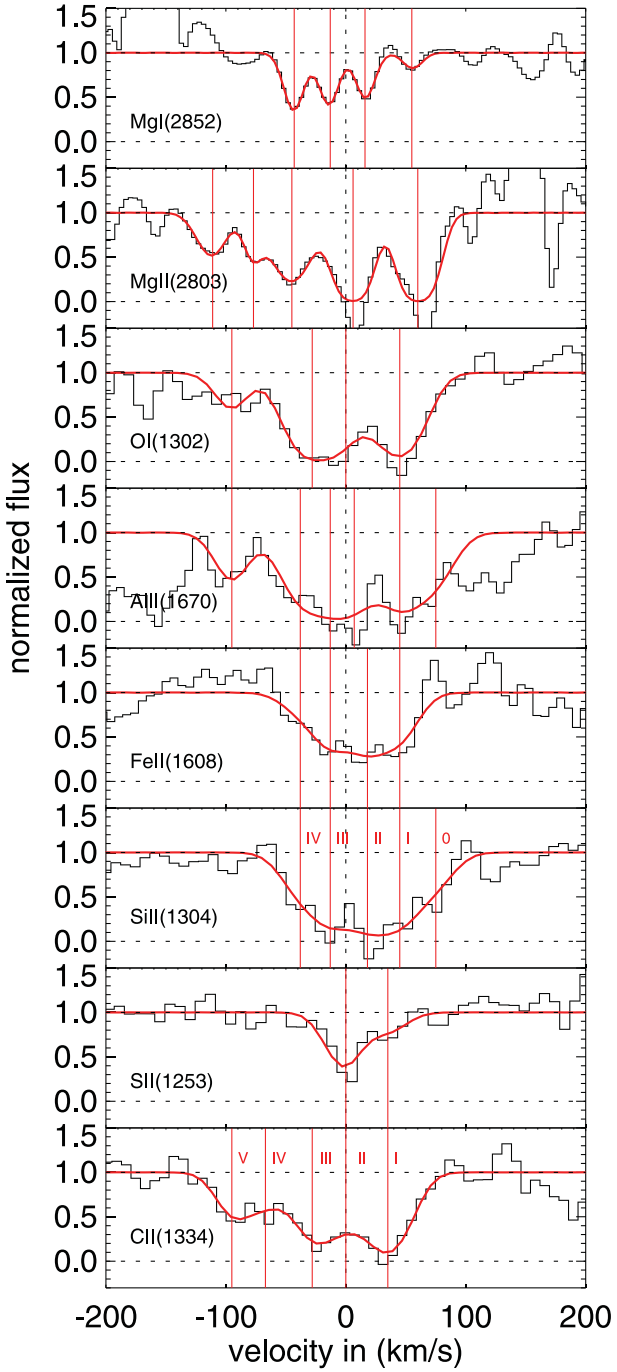

Figure 6. Absorption components for the resonant transitions in the host of GRB 100219A. For Mg II, we show the fit to all components but do not consider the two redmost components for the column density due to contamination by the neighbouring skyline.

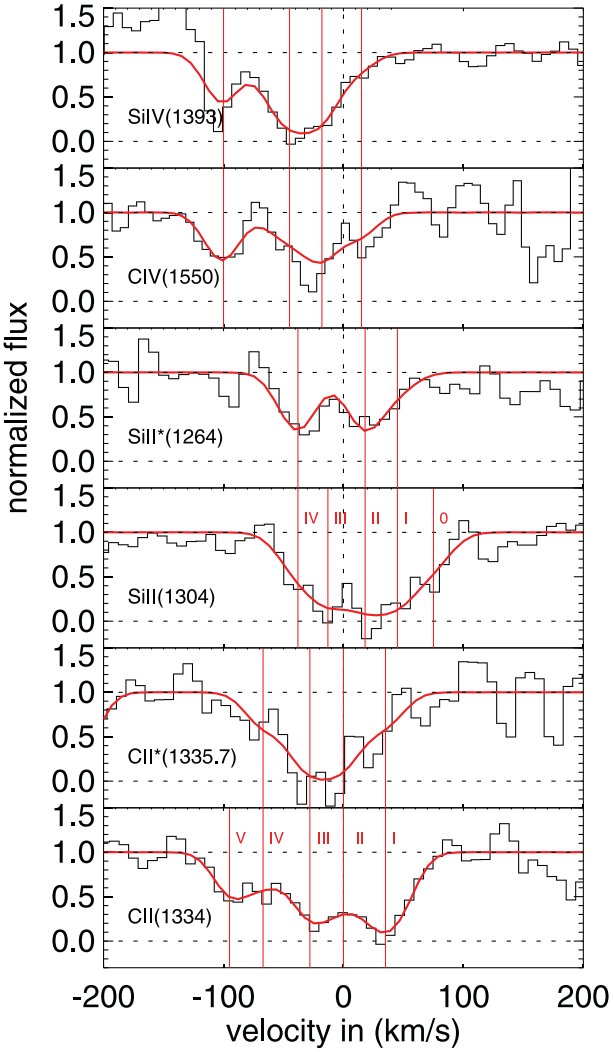

Figure 7. Comparison between the absorption component of the low-ionization, fine-structure and high-ionization lines. For the low-ionization lines, the strongest absorption component is component I, while for the high-ionization lines and fine-structure transitions, component III and IV are the strongest. Component V is rather strong for the high-ionization lines but is absent in the fine-structure lines and weaker in the resonant absorption lines.

and massive SF (Lehnert et al. 2009) have been proposed. Förster-Schreiber et al. (2009) conclude from galaxies in the SINS survey that around 30 per cent of the galaxies at $z = 1$–3 are rotationally supported, but turbulent discs probably indicate that they have completed most of their formation process, while another 30 per cent might be galaxy mergers. However, Law et al. (2009) suggest that clumping of gas during the formation process and subsequent infall to the centre of the galaxy can explain the observed velocity field and mimic the appearance of a velocity field produced by a merger. On the other hand, the reverse is true as Robertson et al. (2006) show that a gas-rich merger can mimic a velocity field resembling a disc rotation. Both merging and gas infall have to play an even larger role for galaxies at $z \sim 5$.

The complicated velocity field observed for the host of GRB 100219A might be explained either with the infall of metal-rich material on to the galaxy or with the galaxy being involved in a large merger with another galaxy. Infalling gas as proposed for the velocity structure of other high-redshift galaxies should, according to the models, be largely pristine gas; hence, this scenario seems less likely for our galaxy and the velocity field might indeed point to an ongoing merger. The large velocities observed for Mg II could also indicate some sort of galactic outflow, like it has been found for GRB hosts at low redshifts (Thöne et al. 2007). Future studies have to show whether the velocity structure of the ISM in high-redshift galaxies and GRB hosts is more complex than the one of lower redshift galaxies.

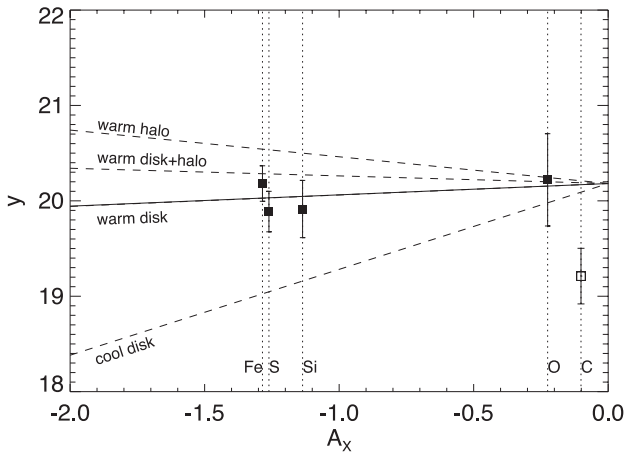

Figure 8. Abundances measured in GRB 100219A and plotted according to the dust depletion method described in Jenkins (2009). A_X shows the propensity of an element to convert from gas to solid which roughly correlates with element condensation temperature and is hence fixed for each element. The *y*-axis shows the column density convolved with several parameters that Jenkins (2009) obtained by fitting several sightlines in the MW such that for a certain depletion along a sightline, the elements lie on a straight line with slope F^* (the 'depletion factor'). The metallicity is then obtained by the difference between log N_H and the intersection of the linear fit with the *y*-axis (the normalization). The solid line shows the linear fit to our data, resulting in a depletion factor of $F^* = 0.12$ and a metallicity of ~ -1.04. The dashed lines show an abundance pattern according to different types of sightlines as described in Savage & Sembach (1996), assuming the same metallicity of -1.04. C was not included in the fit.

4 SED FROM X-RAY TO IR

The broad wavelength coverage of X-shooter also enables the derivation of the absolute extinction curve in combination with the X-ray data assuming that the intrinsic afterglow spectrum is a power law or a broken power law (see e.g. Watson & Jakobsson 2012). The flux calibration of our spectrum can be considered reliable between 7000 and 23 000 Å, beyond that the flux of the afterglow is very low and we have to disregard this part of the spectrum. Below 7000 Å, the spectral flux is decreased due to the Lyα forest. As a consistency check for the flux calibration of the spectrum, we also compare the continuum with the fluxes obtained from our GROND photometry at the time of the spectrum (mid-time around 13.2 h after the burst). The spectral continuum has been raised by a factor of 1.5 to match the photometric data which can be explained by slit losses. As found by our group in previous reduction (see e.g. Sparre et al. 2011), the relative flux calibration is reliable even at these flux levels while the absolute calibration may need to be adjusted with photometry.

In order to cover a broader wavelength range, we also include the X-ray spectrum from X-ray Telescope (XRT) on *Swift*. The XRT began observing the field at 15:18:45.0 UT, 178.5 s after the BAT trigger (Rowlinson et al. 2010). The *Swift* XRT observed GRB 100219A from 182 s to 88.5 ks for a total of 8.3 ks. The data are mainly in photon counting mode, plus 23 s in windowed timing mode. The light curve can be modelled with an initial power-law decay with an index of $\alpha_1 = 1.53^{+0.28}_{-0.22}$, followed by a break at 785 s to $\alpha_2 = 0.57 \pm 0.06$ and a final steepening at $\sim 4 \times 10^4$ s (Rowlinson 2010). A flare is present around 1300 s and another smaller one at $\sim 2 \times 10^4$ s.

We extract a spectrum using the *Swift* XRT spectrum repository (Evans et al. 2009) in the time interval 5000–80 000 s, during which the X-ray spectral hardness ratio remained constant (and therefore we do not expect strong spectral variations), resulting in 5.7 ks effective exposure time. The resulting X-ray spectrum is rebinned to have at least 7 counts per energy bin and has been fitted using the Churazov weighting scheme within the spectral fitting package XSPEC (v.12.7.0). The latest XRT response matrix was used (v.013). We model the observed spectrum with an absorbed power-law model. Our fit includes two absorbers, one Galactic (fixed to 6.5×10^{20} cm^{-2}; Kalberla et al. 2005) and one intrinsic to the GRB host galaxy at $z = 4.667$ (we adopt the *phabs* model). The resulting fit is good with a reduced $\chi^2_{red} = 1.1$ for 33 d.o.f. The photon index is $\Gamma = 1.57^{+0.2}_{-0.13}$ (90 per cent confidence level for one interesting parameter) and the intrinsic column density is $N_{HX}(z) = (3.1^{+3.9}_{-2.7}) \times 10^{22}$ cm^{-2}. The mean 0.3–10 keV

Table 4. Metallicities of all GRB hosts from the best fit, values from the literature have all been corrected using the latest solar abundances from Asplund et al. (2009), limits were not corrected. Corrections compared to previous works on solar abundances are <0.05 for values based on Asplund, Grevesse & Sauval (2005) and <0.1 compared to Grevesse & Sauval (1998) for all elements used except S, for which a correction of −0.21 had to be applied. Data from the literature are [1] Savaglio (2006), [2] Vreeswijk et al. (2006), [3] Prochaska et al. (2007), [4] Vreeswijk et al. (2004), [5] Watson et al. (2006), [6] Berger et al. (2006), [7] Ledoux et al. (2009), [8] Piranomonte et al. (2008), [9] Kawai et al. (2006), [10] Fynbo et al. (2006), [11] Chary et al. (2007), [12] Thöne et al. (2011), [13] Eliasdottir et al. (2009), [14] Ledoux et al. (2009), [15] De Cia et al. (2011), [16] Prochaska et al. (2009), [17] D'Elia et al. (2011), [18] D'Avanzo et al. (2010), [19] de Ugarte Postigo et al. (2012). For GRB 050904 ($z = 6.29$) we adopt a new, lower value, as described in Section 6.1. Data for GRBs observed with X-shooter published until now (comprising all bursts observed until the end of 2010) are from [20] de Ugarte Postigo et al. (2010b)/Fynbo (private communication), [21] D'Elia et al. (2010) and [22] Skúladóttir (2010).

GRB	Redshift	*X*	[*X*/H]	Reference
Literature				
000926	2.038	Zn	-0.13 ± 0.21	[1]
011211	2.142	Si	-0.90 ± 0.50	[2]
030226	1.987	Fe	-1.05 ± 0.18	[3]
030323	3.372	S	-1.26 ± 0.20	[4]
050401	2.899	Zn	-1.0 ± 0.4	[5]
050505	4.275	S	-1.2 ± 0.1	[6]
050730	3.968	S/Si	-2.18 ± 0.11	[7]
050820	2.615	S	-0.63 ± 0.11	[3]
0050922C	2.200	S	-2.03 ± 0.14	[3, 8]
050904	6.295	S	-1.6 ± 0.3	[9], this work
060206	4.048	S	-0.84 ± 0.10	[10]
060223	4.41	S	>-1.8	[11]
060510B	4.94	S	-0.85 ± 0.10	[11]
060526	3.221	S	-1.09 ± 0.24	[12]
070802	2.455	Zn	-0.46 ± 0.38	[13]
071031	2.692	Zn	-1.73 ± 0.05	[14]
080210	2.641	Si	-1.21 ± 0.16	[15]
080310	2.427	O	>-1.91	[14]
080413A	2.435	Zn	-1.60 ± 0.16	[14]
080607	3.037	O	~ 0.2	[16]
081008	1.9683	Zn	-0.52 ± 0.11	[17]
090205	4.650	S	>-0.57	[18]
090516	4.11	Si	>-1.2	[19]
X-shooter				
090313	3.373	Fe	-1.7 ± 0.3	[20]
090226A	2.107	S	-2.0 ± 0.1	[21]
090809	2.73	Si	-0.76 ± 0.09	[22]
100219A	4.667	S	-1.1 ± 0.2	This work
100425A	1.755	Fe	-1.58 ± 0.18	[22]

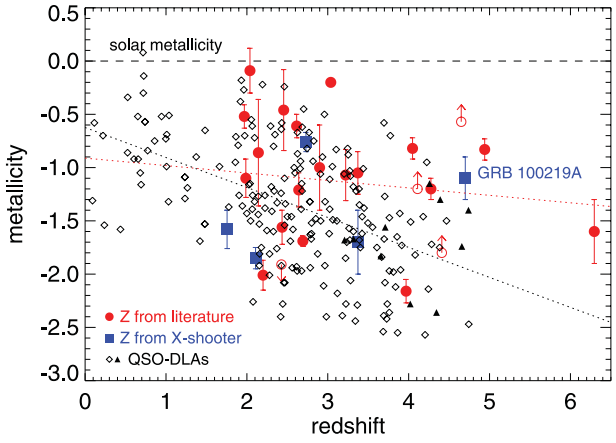

Figure 9. Currently published GRB host metallicities from absorption lines (filled dots) including X-shooter metallicities (filled squares) compared to QSO-DLA metallicities (diamonds and filled triangles), error bars are omitted for clarity. References to the metallicities of GRB hosts are found in Table 4. QSO-DLA metallicities are from Rafelski et al. (2012) (filled triangles) and older samples recompiled in Rafelski et al. (2012) (empty diamonds).

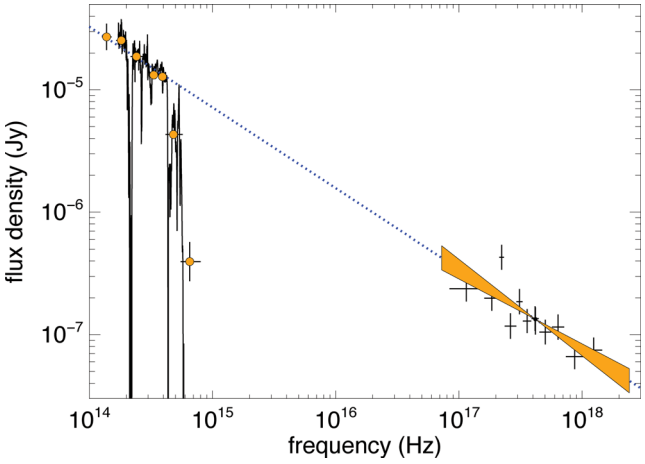

Figure 10. Broad-band SED fitting of the X-shooter optical-NIR and X-ray spectrum. The black line shows the X-shooter spectrum corrected for an extinction of $A_V = 0.13 \pm 0.05$ mag using an SMC extinction law. The orange filled symbols overplotted on the optical/IR spectrum show photometric points from GROND (see Table 1). The spectral slope with errors from the X-ray data is indicated by the shaded region. The extrapolation of the optical slope is consistent with the X-ray spectrum (dotted line). X-rays and optical data have been scaled to the corresponding flux at the time of the observations of the X-shooter spectrum using interpolations of photometric data from the X-ray and optical light curves.

(unabsorbed) X-ray flux during the selected interval is 2.5×10^{-12} erg cm^{-2} s^{-1}.

The best fit to the X-shooter continuum results in an extinction of $A_V = 0.13 \pm 0.05$ mag and an SMC extinction law (see Fig. 10). The moderate extinction from the afterglow continuum is in line with the moderate dust depletion derived in Section 3.3. Dust depletion seems to be common in GRB hosts (see, e.g., Savaglio 2006) and higher than that in QSO-DLAs despite the generally low extinction found from SED fits to the afterglow, the reason for which is still debated. The slope of the SED is $\beta_{\rm opt} = 0.66 \pm 0.13$ consistent with the slope from X-rays of $\beta_{\rm X} = 0.57$ ($\beta = \Gamma - 1$) (see also Mao et al. 2012). To obtain a reasonable value for the electron distribution index p, this slope implies that the cooling break $\nu_{\rm c}$ according to the fireball model (see e.g. Sari, Piran & Narayan 1998) has to lie bluewards of the X-shooter spectrum and $\beta = (p - 1)/2$ with $p = 2.2$. Fixing the slope in the X-rays to the one from the optical spectrum, we obtain an intrinsic absorption of $N_{\rm HX}(z) = (5.1^{+3.7}_{-2.3}) \times 10^{22}$ cm^{-2} (90 per cent confidence level) and $\chi^2_{\rm red} = 1.1$.

The column density derived from X-rays is about one order of magnitude higher than the column density of H I as derived from the optical of $\log N = 21.14$ (see Table 2). In fact, the X-ray column density is above the average for *Swift* GRBs but comparable to the mean for $z > 4$ GRBs of $\log N_{\rm HX} \sim 22.5$ following the trend of increasing column density with redshift (Campana et al. 2010). This is partly an observational effect (at higher redshifts, a larger column density is needed for it to even be detected) but probably also due to an increase in intervening absorbers contributing to the total absorbing column. Gas-to-dust and metal-to-dust ratios for GRB 100219A are high as it is generally the case for GRBs (Watson & Jakobsson 2012), above the values for the Local Group (Zafar et al. 2011). This is usually explained by ionization of H I and in particular dust destruction by the GRB (Watson et al. 2007; Fynbo et al. 2009; Campana et al. 2010). Ionization by the GRB would also explain the very large difference between optical and X-ray column densities (about a factor of 10), as generally found for GRBs, since X-ray absorption is not affected by ionization and hence most metals are found in highly ionized states due to the absence of a large column density of moderately ionized metals (Schady et al. 2011).

5 THE INTERVENING SYSTEM

Despite the high redshift of the GRB, we only detect one intervening system at a redshift of $z = 2.180$ which might be a consequence of the low S/N of the spectrum. A second intervening system at $z = 1.8$ that had been claimed in de Ugarte Postigo et al. (2010a) could not be confirmed in our refined analysis. We are not able to detect any possible absorption lines from the nearby galaxy at $z = 0.25$. The redmost absorption transitions from the ISM commonly observed are Ca II λλ3933, 3969 Å, which, at $z = 0.25$, still lie within the Lyα forest of the GRB absorption system, the weaker NaD doublet λλ5890, 5895 Å is in a part of the spectrum affected by skylines.

The refined redshift for the intervening system according to the method described in Section 3.1 is $z_{\rm interv} = 2.181\,16 \pm 0.000\,34$. For the $z = 2.181$ system, we securely detect the Mg II doublet λλ2796, 2803, Mg I and Fe II λ2586, whereas the red part of the Fe II λ2600 transition is affected by a skyline. Mg II shows two components separated by 80 km s^{-1} while Mg I and Fe II only show the stronger of the two components, likely due to the lower line strength of those transitions (see Fig. 11 and Table 5).

The redshift path covered by our spectrum is of $\Delta z \sim 2.6$. In the past (e.g. Prochter et al. 2006; Vergani et al. 2009) an excess of both weak and strong intervening absorbers had been found along the line of sight of GRBs compared to those of QSOs. These works consider an upper redshift limit of $z = 2.3$ in order to compare the GRB statistics with the QSO one, based on the SDSS spectra. If we consider this upper limit, the redshift path covered by the GRB 100219A spectrum is $\Delta z = 0.7$ and the detection of one strong Mg II system within this Δz is in line with an excess of the number density of these systems along GRB lines of sight.

Sudilovsky et al. (2007) performed also a statistical study on the GRB foreground C IV absorbers showing that their number is consistent with the one in QSO sightlines. The redshift path covered by our spectrum for the C IV absorbers is $\Delta z \sim 1.15$, while the limit on the C IV column density is $\log N(\rm cm^{-2}) \sim 14$ and 16 for

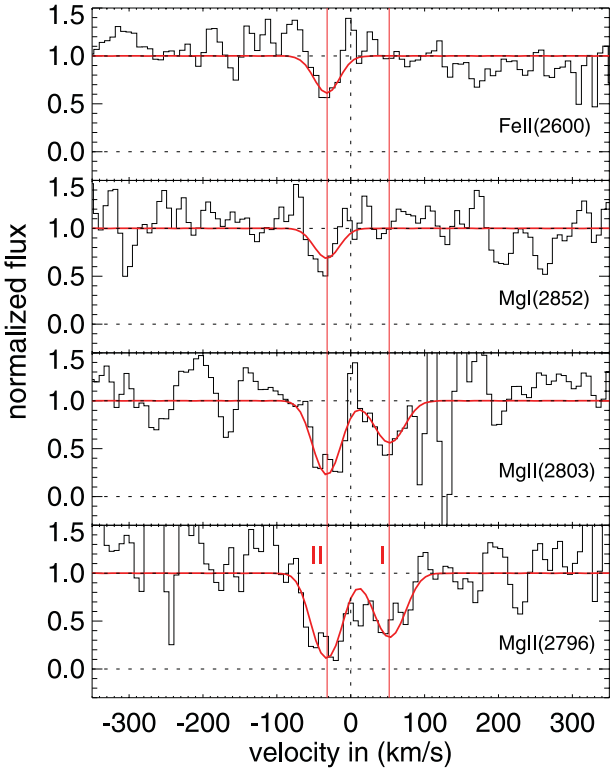

Figure 11. Fits to the two velocity components in the intervening system at $z = 2.181$.

Table 5. Column densities for the two velocity components in the intervening system at $z = 2.181$.

Ion, transition (Å)	I Δv (km s^{-1})	I log N (cm^{-2})	II Δv (km s^{-1})	II log N (cm^{-2})
Mg II 2796, 2803	+52	13.10 ± 0.08	−32	13.56 ± 0.10
Mg I 2852	–	–	−32	12.07 ± 0.14
Fe II 2600	–	–	−32	13.13 ± 0.12

b-parameters of 20 and 5 km s^{-1}, respectively. Sudilovsky et al. (2007) found seven C IV systems in agreement with these limits within $\Delta z \sim 2.25$, whereas we find none. We note that our redshift range for C IV absorbers of $3.5 \lesssim z \lesssim 4.7$ is different from that of Sudilovsky et al. (2007, $1.5 \lesssim z \lesssim 3$) and no statistics are available for GRB C IV absorbers within this range. Thanks to the large spectral coverage of X-shooter, it will be possible to build a statistically significant and homogeneous sample of intervening absorbers and extend the studies to much higher redshifts.

6 GRB 100219A IN THE CONTEXT OF HIGH-REDSHIFT GALAXY ABUNDANCES

6.1 GRBs at $z > 4$

To date, 273 redshifts of GRBs have been determined (of these, 209 were detected by *Swift*).[4] This number includes secure photometric redshifts and redshifts determined using emission lines from the host galaxy, but not limits from optical/UV detections. Only 23 (8.4 per cent) of those 273 bursts are above $z = 4$ (20 bursts or 9.5 per cent for *Swift)*, of which 4 were obtained by photometric redshift methods. Eight (2.9 or 3.8 per cent for *Swift* only) are at $z > 5$ of which two are photometric redshifts. The current records are $z = 8.2$ for GRB 090423A (spectroscopic; Salvaterra et al. 2009; Tanvir et al. 2009) and $z = 9.4$ for GRB 090429A (photometric; Cucchiara et al. 2011), which make them one of the farthest objects detected in the Universe.

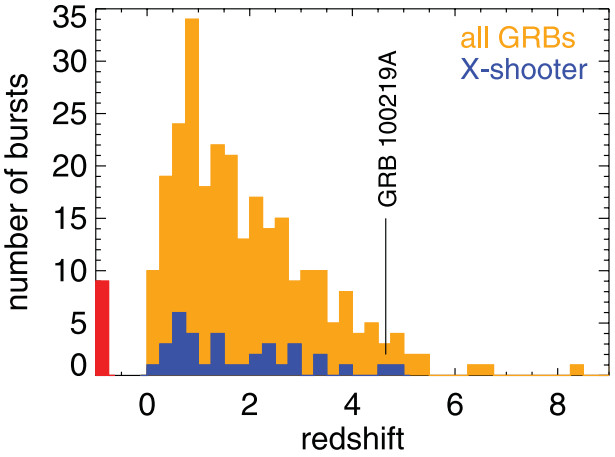

Figure 12. Redshift distribution of all GRBs with secure redshifts (spectroscopic and photometric, orange) and the same for GRBs observed with X-shooter (blue histogram). X-shooter spectra where the redshift could not be determined are shown in red.

In the past, it had been estimated that a much larger fraction of GRBs might be observed at redshifts beyond 4and5 (Bromm & Loeb 2002, 2006) and, taking into account the sensitivity of *Swift*, at least 10 per cent should be at $z > 5$. It had been suggested that part of the high-redshift GRBs were missed due to the lack of NIR observations and high-sensitivity NIR spectrographs to determine redshifts. However, Greiner et al. (2011) detected afterglows with GROND for more than 90 per cent of the GRBs if observations were possible early enough, although they did not detect, e.g., GRB 090429B at $z = 9.4$ (Cucchiara et al. 2011). Their redshift distribution is similar to the overall distribution, leaving little room for a significant high-redshift population being missed by observations. X-shooter has to date determined 26 redshifts (2 or 8 per cent at $z > 4$) and the redshift distribution for GRBs observed with X-shooter is similar to the distribution for all GRBs (see Fig. 12).[5] Observational constraints would also not explain the scarcity of GRBs between redshifts 4 and 6, which are still easily detectable with optical spectrographs.

The reason for this relatively low rate might be related to the capability of *Swift* (and other past and current gamma-ray observatories) to detect high-z GRBs. Time dilation stretches the emitted flux over a longer time interval, making rate triggers more difficult (in fact, GRB 100219A was discovered in an image trigger). In addition, the peak emission of long, already intrinsically soft GRBs gets shifted to even lower bands, so that part of the flux falls below the BAT bands. In fact, Gorosabel et al. (2004) concluded that the *INTEGRAL* satellite with its different energy bands should detect more GRBs at high z than *Swift*. Several authors have also suggested that

[4] http://www.mpe.mpg.de/ jcg/grbgen.html and the GCN archive as on 2012 October 9.

[5] Since the first submission of this publication, X-shooter had detected a GRB with higher redshift than GRB 100219A, GRB 111008A at $z = 4.9898$ (Wiersema et al. 2011).

Table 6. Properties of all $z > 4$ GRBs. Those with only a photometric redshift, GRB 050814 (Jakobsson et al. 2006), GRB 071025 (Perley et al. 2010), GRB 080916C (Greiner et al. 2009c), GRB 080825B (Krühler et al. 2011a) and GRB 090429A (Cucchiara et al. 2011), are not included. Metallicities in bold are the ones adopted throughout the paper. References for values from the literature are [1] Andersen et al. (2000), [2] Berger et al. (2006), [3] Kawai et al. (2006), [4] Totani et al. (2006), [5] Berger et al. (2007) [6] Chary et al. (2007), [7] Thöne et al. (2008), [8] Price et al. (2007), [9] Ruiz-Velasco et al. (2007), [10] Greiner et al. (2009b), [11] D'Avanzo et al. (2010), [12] Greiner et al. (2009a), [13] Patel et al. (2010) [14] Tanvir et al. (2009), [15] Salvaterra et al. (2009), [16] Chary et al. (2009), [17] de Ugarte Postigo et al. (2012), [18] Chornock et al. (2010), [19] Cenko et al. (2010a), [20] Wiersema et al. (2011), [21] Fynbo et al. (in preparation).

GRB	z	log $N_{\rm H\,I}$ ($\rm cm^{-2}$)	[Z/H]	Host $M_{\rm B}$ (AB mag)	Reference	Comment
000131	4.50	–	–	–	[1]	Only Lyα detected
050505	4.27	22.05 ± 0.1	$\mathbf{-1.2}$ (S), -1.6 (Si), -2.0 (Fe)	–	[2]	–
050904	6.29	21.6	-1.0 (S), -2.4 (C), -2.3 (O), -2.6 (Si)	>-20.5	[3, 4, 5]	
			$\mathbf{-1.6 \pm 0.3}$		This work	Revised metallicity
060223A	4.41	21.6 ± 0.1	<-1.45 (Si), >-1.8 (Si)	>-21.0	[6]	
			$\mathbf{-1.6 \pm 0.2}$			
060206	4.04	20.85 ± 0.1	$\mathbf{-0.86}$ (S), -1.08 (Si), -1.16 (C)	-20.3 ± 0.2	[7]	
060510B	4.94	21.3 ± 0.1	$\mathbf{-0.85}$ (S), >-0.8 (Fe)	-20.9 ± 0.2	[6, 8]	
060522	5.11	21.0 ± 0.3	–	>-26.4	[6]	Only Lα detected
060927	5.47	$\sim$22.5	–	–	[9]	Low S/N spectrum
080129	4.35	–	–	–	[10]	Low S/N spectrum
090205	4.64	20.73 ± 0.05	$\mathbf{> -0.57}$ (S)	-22.5 ± 0.1	[11]	
080913	6.69	19.84	–	–	[12, 13]	
090423	8.2	–	–	>-19.9	[14, 15, 16]	
090516	4.11	21.73 ± 0.02	$\mathbf{> -1.2}$ (Si)	–	[17]	
100302A	4.81	–	–	–	[18]	
100219A	4.67	21.14 ± 0.04	$\mathbf{-1.1}$ (S), -1.4 (Si), -1.9 (Fe), -1.0 (O)	-21.0 ± 0.5	This work	
100513A	4.77	–	–	–	[19]	
111008A	4.98	$\sim$22.4	(~ -2.0)	–	[20, 21]	[*M*/H] preliminary

without a luminosity evolution of GRBs it is unlikely that we would detect GRBs at that redshift at all (e.g. Salvaterra et al. 2007), but determining the luminosity function of high-redshift GRBs suffers from small number statistics.

Another unknown factor is the evolution of the star formation rate (SFR) at high redshifts. The peak of the SF is expected to be around $z \sim 2$, and it is not yet known how the SF evolves at redshifts beyond $z \sim 4$. Several attempts have been made to determine the cosmic SFR using GRBs (see, e.g., Yüksel et al. 2008; Kistler et al. 2009) indicating a shallower decay towards higher redshift than derived by galaxy SF measurements. The redshift distribution of *Swift* GRBs at high redshifts can be well explained by a constant cosmic SF density from redshift 3.5 onwards (Jakobsson et al. 2006).[6] This could be explained if GRBs preferentially select low-metallicity regions. Which of the effects, an evolution of the luminosity function, a metallicity selection effect or a larger SFR at higher redshifts, is the one responsible for the observed evolution that cannot be determined at present.

In Table 6 we list the properties of all GRBs with $z > 4$ with spectroscopic observations since the discovery of GRB afterglows. Of the 17 GRBs at $z > 4$ with spectroscopic redshifts, 5 have measured metallicities, 3 more have derived limits. For GRBs with $4 < z < 5$, the majority has values or limits for the metallicity (8 out of 12), for the remaining four GRBs at least two seem to have good enough spectra to determine a metallicity but are not yet published (GRB 100302A, Chornock et al. 2010; GRB 100513A, Cenko et al. 2010b). For GRB 090516 (de Ugarte Postigo et al. 2012) we list the metallicity determined from the EW of Si II λ1808 assuming that it lies on the linear part of the Curve-of-Growth (CoG). This spectrum shows unusually strong lines, so that even the weak Si II λ1808 line is mildly saturated and the real metallicity is probably $\sim$0.3–0.4 dex higher taking typical values for the *b*-parameter to be around 20–30 km $\rm s^{-1}$.

At $z > 5$, determining metallicities gets increasingly difficult, only one metallicity has been reported for a GRB beyond $z = 5$, GRB 050904 (Kawai et al. 2006). However, their metallicities derived from C, Si, O and S differ by more than an order of magnitude and they adopted the value derived from S which is the highest of all four elements. They argue that this might be due to dust depletion; however, e.g. Si should track S rather close. Kann, Masetti & Klose (2007) and Zafar et al. (2010), however, found no indication for dust depletion from the SED of the afterglow itself (but see Stratta et al. 2007; Stratta, Gallerani & Maiolino 2011).

We reinvestigate the spectra of GRB 050904 from Kawai et al. (2006) which have also been studied in Zafar et al. (2010) and find different EWs for S II λ1253 and Si II λ1260 (2.7 and 13.0 Å observer frame, respectively), while S II λ1259 is blended with Si II λ1260 and cannot be measured. All lines except S II listed in Kawai et al. (2006) are completely saturated, also including another Si II line at λ1304 not listed in the paper. The saturation makes a curve-of-growth fit as mentioned in Kawai et al. (2006) impossible; however, the column densities of Si II, O I and C II are definitely higher than listed in the paper. Taking the EW from S II λ1253 and assuming a (reasonable) *b*-parameter of $\sim$ 35 km $\rm s^{-1}$, we obtain a column density of around log $N \sim 15.3$, 0.3 dex lower than listed in Kawai et al. (2006). Totani et al. (2006) reinvestigated the DLA column density of GRB 050904 and found a slightly higher value of log $N_{\rm H\,I} = 21.6$.

Together, this gives a revised metallicity of [*M*/H] ~ -1.6 and we give a conservative 3σ error of 0.3 dex. This is also in line with the findings of Campana et al. (2007) deriving a metallicity of

[6] For a recent update, see http://www.raunvis.hi.is/~pja/GRBsample.html

$[M/H] > -1.7$ from X-ray spectra. Dust depletion is likely not playing a major role since the metallicities from different elements are more similar than previously thought, although the definite values cannot be determined.

6.2 Comparison between high-redshift GRBs and QSO absorbers

Observations of QSO absorbers at $z > 4$ become difficult since current surveys only detect the most luminous ones. The intergalactic medium at those redshifts is almost opaque for Lyman α photons. This makes it difficult to detect and measure the column density of DLAs in the sightline, which in turn hampers the direct determination of the metallicity. The largest samples of QSO-DLAs and their properties (Prochaska et al. 2003; Prochaska, Herbert-Fort & Wolfe 2005; Dessauges-Zavadsky et al. 2006; Ledoux et al. 2006; Rafelski et al. 2012) comprise a number of systems up to $z \sim 4.8$ (see Fig. 9). Becker et al. (2011) determined properties of $5 < z < 6$ QSO absorbers but could only indirectly derive the metallicity of those systems.

QSO-DLAs show a decrease in metallicity with redshift (Dessauges-Zavadsky et al. 2006; Prochaska et al. 2007) with a large scatter at each redshift. There seems to be a 'metallicity floor' at $[Z/H] \sim -2.6$ explained by a rapid early enrichment due to SF. In Fig. 9 we plot all GRB host metallicities reported in the literature together with metallicities from the large QSO-DLA sample of Prochaska et al. (2003) and fit a linear evolution to the data for each sample. As has been pointed out in the past (Fynbo et al. 2006; Savaglio 2006), GRB hosts have larger metallicities and less evolution with redshift compared to QSO-DLAs. At $z > 4$, this becomes clearly evident as the mean GRB-DLA metallicity is about one order of magnitude larger than the mean of QSO-DLAs. Albeit a large scatter exists at all redshifts, the mean GRB host metallicity seems to show a much shallower evolution compared to that of QSO-DLAs.

At $z > 5$, the ionization fraction of QSO absorbers is very low and Si IV and C IV are hardly ever detected (Becker et al. 2011). However, this is consistent with the ionization fraction at lower redshifts due to a general decrease in column densities which makes the column densities of Si IV and C IV fall below the detection limit. GRBs with their generally higher metallicity should therefore show more Si IV and C IV, which is the case. GRBs do not exhibit any trend with redshift, neither in the overall abundance, nor is there any evident change in the ionization fraction and at high redshifts as shown in Fig. 13 for carbon. Special cases such as the highly ionized material around GRB 090426 (not shown in the plot) do not reflect this global picture since they likely probe very special environments (Thöne et al. 2011).

The distribution of GRB-DLA H I column densities has a higher mean value than those of QSO-DLAs and extends to much higher densities (e.g. Fynbo et al. 2009). It has been suggested that the cosmic neutral hydrogen density reaches a maximum around $z \sim 3.5$ and decreases for lower redshifts (Prochaska et al. 2005), since the gas is consumed or expelled from galaxies, while the evolution at $z > 4$ is still inconclusive. The frequency distribution of DLAs and sub-DLAs shows little evolution but the slope might change slightly implying more sub-DLAs and less high column density systems at high redshifts (Prochaska et al. 2005; Guimarães et al. 2009). In Fig. 14 we plot log $N_{\rm H\,I}$ for all GRBs for which this value is available from the literature and determine the mean and standard deviation at three redshift bins excluding sub-DLAs (log $N_{\rm H\,I} < 20.3$). The mean column densities are log $N_{\rm H\,I} = 21.76 \pm 0.38$ for $2 < z < 3$, 21.80 ± 0.62 for $3 < z < 4$ and 21.42 ± 0.56 for $z > 4$; hence, there is no evolution with redshift. Only a few GRBs with sub-DLA column densities have been found, all at $z < 4$, but this is consistent with the number expected from the overall H I distribution. It seems that GRB hosts have high content of neutral gas irrespective of redshift which gives them a large reservoir for the formation of stars.

It is still debated whether QSO-DLAs (and GRB-DLAs) show an enhancement in α elements (O, Ne, Mg, Si, Ca), produced in massive stars, versus iron-peak elements (Fe, Ti, Zn), which primarily come from Type Ia SNe. An overabundance of α elements

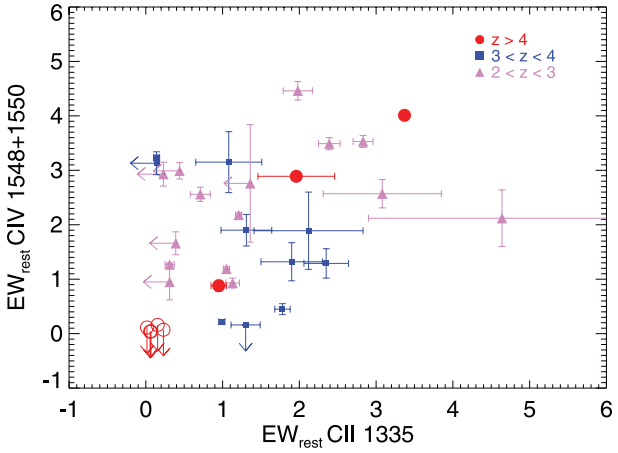

Figure 13. Ionization of C in GRB-DLAs at three different redshift bins (filled symbols) and the comparison to measurements in $z = 5$and6 QSO absorbers (empty circles) from Becker et al. (2011). GRB-EWs are taken from the low-resolution *Swift* sample of Fynbo et al. (2009) and its extension until 2009 September published in de Ugarte Postigo et al. (2012). The C IV EWs for the GRB sample include both lines of the λλ1548, 1550 doublet, upper limits of the QSO sample are 2σ limits on C IV λ1548. Values for QSOs for the other two redshift bins are not shown for clarity and we refer to fig. 13 in Becker et al. (2011). GRB-DLAs do not show any evident trend with redshift, neither in line strength nor in the ionization fraction and have higher line strengths than QSO absorbers at $z > 4$.

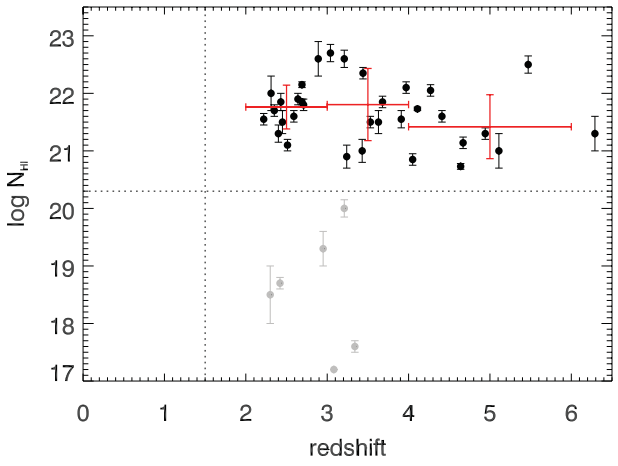

Figure 14. Column density of *Swift* GRB-DLAs versus redshift from the sample of Fynbo et al. (2009) and later published values from the literature. The vertical dotted line indicates the detection limit of Lyα from the ground. The grey points denote column densities, overplotted are the average column density and standard deviation in three redshift bins ($2 < z < 3$, $3 < z < 4$ and $z > 4$). For the average column density we exclude sub-DLA systems (log $N_{\rm H\,I} < 20.3$, horizontal dotted line) since they might probe different environments; the values are plotted with empty circles. The GRB-DLA H I column density shows a large scatter at all redshifts but no trend towards lower column densities at higher redshifts as observed for QSO-DLAs.

is expected for young star-forming regions and a corresponding correlation between metallicity and [α/Fe] has been found for MW stars. Determining the [α/Fe] ratio is complicated by differential dust depletion since Fe is more sensitive to dust depletion than e.g. Si. All studies of QSO-DLAs have found a statistically significant α enhancement (e.g. Wolfe, Gawiser & Prochaska 2005; Dessauges-Zavadsky et al. 2006). It has been claimed that, correcting for dust depletion, the enhancement disappears (e.g. Pettini et al. 2002, but see also Savaglio, Panagia & Stiavelli 2000). However, a mean positive ratio of [α/Fe] was found even for very metal poor (hence dust-free) systems (Wolfe et al. 2005) as well as for dust-free systems as determined by [Fe/Zn] (Dessauges-Zavadsky et al. 2006, Zn is supposed to be little affected by dust depletion). Extinction determined from the spectral continuum is generally low for GRB-DLAs and QSO-DLAs with somewhat higher values for GRB-DLAs. However, dust depletion and extinction are not always tightly correlated, which could be caused by a 'patchy' distribution of the dust along the line of sight. For GRB 100219A, we obtain a ratio [α/Fe] of +0.39 (Si) and +0.76 (S). Si is only mildly depleted while S can be considered as little affected by depletion so the enhancement might be real. An enhancement has also been found for other GRBs (Savaglio 2006) but the sample is still too small to make a definite conclusion or to investigate a possible redshift dependence.

6.3 The mass–metallicity relation at high redshifts

In the local Universe, galaxies follow a correlation between stellar mass content and metallicity and, with a less tight correlation, between (*B*-band) luminosity and metallicity (*L*–*Z* and *M*–*Z* relations). A corresponding mass–metallicity relation has been derived from the large SDSS sample by Tremonti et al. (2004), with metallicities derived from strong emission lines of the luminous gas in the galaxy. Deriving reliable stellar mass content of galaxies usually requires broad-band SED fitting or at least a detection in the rest-frame *K* band, which makes it difficult to derive the masses at higher redshifts. Emission-line metallicity measurements at redshifts beyond $z \sim 1$ require the use of high-sensitivity NIR spectrographs. In the past few years, the local *M*–*Z* (or *L*–*Z*) relation has been extended to a redshift of $z \sim 3.5$ (see Mannucci et al. 2009 and references therein).

It has become clear that the *M*–*Z* relation at increasing redshift changes towards lower metallicities for a given stellar mass (Savaglio et al. 2005; Erb et al. 2006; Kewley & Ellison 2008; Mannucci et al. 2009). This effect is largely due to the enrichment with metals over time but the metal enrichment of galaxies is also a complex function of SF efficiency and feedback with the intergalactic medium. GRB hosts fall below the mass–metallicity relation for field (SDSS) galaxies (Han et al. 2010; Kocevski & West 2011) which had been taken as evidence for GRB hosts being biased towards lower metallicities, possibly because GRBs need low-metallicity environments (Woosley & Heger 2006). However, Mannucci et al. (2010) established a connection between metallicity and SFR showing that star-forming galaxies have on average lower metallicities, which can explain part of the discrepancy to field galaxies (Kocevski & West 2011). Similar to the *M*–*Z* relation, the *L*–*Z* relation also shows an evolution with redshift, but the overall correlation is less tight. At low redshifts, the *L*–*Z* correlation is better constrained, probably due to a tight correlation between mass and luminosity. At higher redshifts, the scatter in the mass-to-light ratio between *B*-band magnitude and mass is rather large (see Erb et al. 2006) and also steeper than in the local Universe, which makes the *L*–*Z* relation at $z > 2$ rather unconstrained.

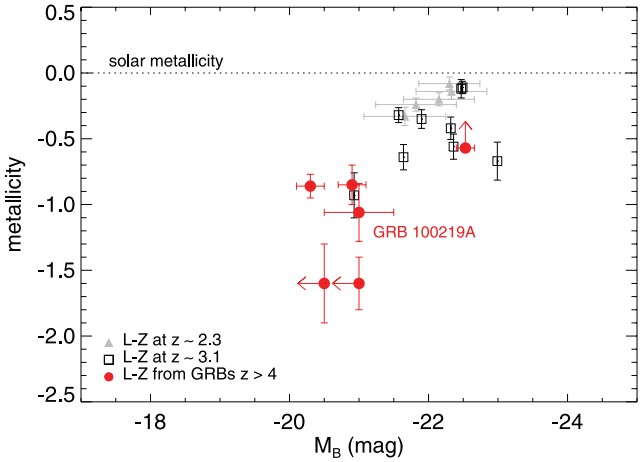

Figure 15. Luminosity–metallicity relation of $z > 4$ GRBs compared to field galaxy samples at slightly lower redshifts. Galaxy data are from Erb et al. (2006) for $z \sim 2.3$ and from Mannucci et al. (2009) for $z \sim 3.1$.

Metallicities of GRB hosts using emission lines have only been determined for a few hosts up to $z \sim 2$, which will be significantly improved with X-shooter in the near future. At high redshifts, we have to rely on absorption-line metallicities, but we have to be aware that the metallicity derived from the luminous, hot gas of star-forming regions might not be the same as derived from the cold gas of the galaxy ISM. We collected all reported host detections and upper limits for $z > 4$ GRBs from the literature (see Table 6). Due to the lack of broad-band modelling, we only investigate the *L*–*Z* relation since the relation between *B*-band magnitude and stellar mass seems to change with redshift and is still uncertain at higher redshifts; therefore, deriving a stellar mass would introduce additional errors. For GRB 050904, GRB 060223A, GRB 060510B and GRB 090423, rest-frame *B*-band magnitudes were given in Chary et al. (2007, 2009) from *Spitzer* observations. For GRB 100219A, we take the i'-band detection from Section 2.2. Magnitudes given in other bands were transformed to rest-frame *B*-band magnitudes using a rough *k*-correction of the form $k = -2.5(1+\beta) \times \log_{10}(1 + z\,(\lambda_B/\lambda_{\rm init.}))$ with $\lambda_{\rm init.}$ and λ_B as the central wavelength of the original and the *B*-band filter, respectively. We assume a power-law slope for the host SED of the form $F_\nu \propto \nu^\beta$ with $\beta = 0.5$.

Fig. 15 shows the result for GRB hosts with $z > 4$ compared to two other samples for field galaxies of $z \sim 2.3$ (Erb et al. 2006) and $z \sim 3.1$ (Mannucci et al. 2009). GRB 050904 at $z = 6.29$ with our corrected metallicity and GRB 060223A clearly lie below the galaxies at $z \sim 3.1$ while the other four hosts, including GRB 100219A, are consistent with the relation at lower redshifts. The number of high-redshift GRBs is still too low to make any conclusive statement on the *L*–*Z* relation of GRB hosts.

Salvaterra, Ferrara & Dayal (2011) studied the redshift evolution of the mass–metallicity relation from redshift 5 to 10 using galaxy evolution simulations with the GADGET code (Springel 2005). They found considerable enrichment even of the smallest galaxies of up to 1/10 already at redshifts 7 and 8 and probably even higher. The metallicity of $\sim$0.1 $Z_\odot$ for GRB 100219A is fully consistent with chemical evolution models. Comparing the *L*–*Z* relation at $z = 5$ from the simulations of Salvaterra et al. (2011), our GRB hosts at $z = 4$and5 would still fall somewhat below the relation, confirming the trend seen at lower redshifts. Further investigations of the relation with new observations, in particular at $z > 5$, would be highly desirable to study the early chemical enrichment of galaxies and their SF history and ISM feedback.

A direct determination of the *L–Z*/*M–Z* relation of QSO absorbers is difficult to obtain; however, several authors have confirmed a correlation of the velocity spread of, e.g., Si II λ1526 and the metallicity (Ledoux et al. 2006; Prochaska et al. 2008). This correlation seems to decrease with redshift, mostly due to the change in metallicity. The velocity spread is probably related to the dark matter halo mass of the absorbers (Ledoux et al. 2006); hence, the velocity–metallicity relation can be seen as a mass–metallicity relation and the observed trend fits to the *M–Z*/*L–Z* relations found in emission. A tight correlation has also been found for the metallicity versus the EW of Si II λ1526 of QSO-DLAs such that it can be used as a proxy for metallicity if no other measurement is available (Prochaska et al. 2008) and this correlation might also be present for GRB-DLAs, albeit with a different slope and offset. The reason for this correlation might be the underlying velocity–metallicity relation and the suggestion that the EW of saturated absorption lines traces the kinematics of the gas well. The EW of Si II λ1526 of GRB-DLAs does not evolve much with redshift (Fynbo et al. 2009), while it decreases for QSO-DLAs. On the other hand, the velocity spread of, e.g., Si II λ1526 in QSO-DLAs does not show large changes at high redshifts (Prochaska et al. 2005; Becker et al. 2011). The identification of the galaxy counterparts of QSO-DLAs is difficult due to their faintness and the proximity of the QSO; therefore, a direct mass–metallicity or luminosity–metallicity relation for the galaxy counterparts of QSO-DLAs has not been determined yet.

7 CONCLUSIONS

In this paper we presented X-shooter spectra of GRB 100219A at $z = 4.667$ which is the highest redshift at which a high-resolution spectrum has been available until now, allowing a detailed analysis of the abundances in a high-redshift (star-forming) galaxy. The metallicity as determined from sulphur is moderately high with $[S/H] = -1.1$ or 0.1 $Z_{\odot}$, similar to the value found for other GRBs between redshifts 3and4, but 10 times higher than the average metallicity of galaxies found in the sightlines of QSOs at this redshift. There is little evidence for extinction from the afterglow SED and the relative abundances of the detected metal absorption species indicate only a mild dust depletion. This suggests that the α-element enhancement of $[\alpha/Fe] = 0.3$–0.7 we find from Si and S is likely real. The kinematics of low-, high-ionization and fine-structure lines is rather complicated, probably showing an early galaxy in the process of formation or merging with another galaxy. We also detect one intervening system at $z = 2.181$, consistent with the detection rate of intervening absorbers in GRB sightlines.

Studying galaxies and their abundances in the high-redshift Universe is of great importance to our understanding of the cosmic chemical evolution, in particular at redshifts where galaxies were still in the process of formation. Over the last few years, it has become evident that galaxies probed by QSOs and GRBs show somewhat different properties. While GRB hosts have a very shallow metallicity evolution, QSO-DLAs have on average a factor of 10 times less metallicity at $z \sim 4$ and show a steep increase up to $z \sim 2$, where the metallicities of both samples become similar. GRBs also show no evolution in ionization rate (though this is likely also the case for QSO-DLAs) and in the H I average column density and distribution. Probably, GRBs select similar types of galaxies across the history of the Universe, highly star forming and metal poor, while QSO-DLAs probe the average galaxy population.

It has been suggested that both QSO-DLAs and GRB-DLAs might come from the same population of galaxies and the metallicity distribution can be explained by a sightline effect (GRBs probe the dense regions of the galaxy while QSO-DLAs probe the more metal-poor outskirts) combined with a slightly higher average mass for GRB-DLA galaxies. This seems likely since GRB-DLAs also have much stronger lines, hence probing denser regions, and a higher velocity width than QSO-DLAs. It is still unclear into what type of galaxies in the present Universe high-redshift QSO-DLAs develop into, though they are likely not dwarf galaxies (Prochaska et al. 2005). GRB hosts at low redshifts are a diverse mix of star-forming galaxies, from blue compact dwarfs to spiral galaxies.

The picture is somewhat inverted for the mass–metallicity relation of GRB hosts compared to field galaxies. At low redshifts, GRBs select galaxies more metal poor for their mass than average, even after accounting for a possible bias from star-forming galaxies (that have shown to be on average more metal poor). The comparison at higher redshifts is still unclear but the difference might be less pronounced than in the local Universe. It will be an important task to develop a common picture for the galaxy populations probed by different methods in order to get the global picture of galactic chemical evolution.

The evolution beyond redshift ∼5 is still largely unknown since the current detection rate of such high-redshift GRBs is still low. At redshifts approaching the reionization epoch and the formation of the first stars and galaxies, the determination of metallicities and relative abundances is crucial to test the models for high-redshift SF and the formation and evolution of galaxies.

ACKNOWLEDGMENTS

CT acknowledges the hospitality of DARK where part of this work was done and thanks A. Kann and D. Malesani for carefully reading the final manuscript. Thanks to J. X. Prochaska for providing the $N_{H\,I}$ for GRB 090313. This work is based on observations made with X-shooter under the guaranteed time programme 084.A-0260 (PI: Fynbo), GROND at the MPI/ESO 2.2 m telescope and with telescopes at the European Southern Observatory at LaSilla/Paranal, Chile under programme 084.D-0764, PI: Greiner and observations made with the Gran Telescopio Canarias (GTC) at the Spanish Observatorio del Roque de los Muchachos of the Instituto de Astrofísica de Canarias, La Palma under programme GTC43-11B, PI: C. Thöne. This work made use of data supplied by the UK Swift Science Data Centre at the University of Leicester. The 'Dark Cosmology Centre' is funded by the Danish National Research Foundation. Part of the funding for GROND (both hardware as well as personnel) was generously granted from the Leibniz-Prize to Prof. G. Hasinger (DFG grant HA 1850/28-1). JPUF and BMJ acknowledge support from the ERC-StG grant EGGS-278202. TK acknowledges support by the DFG cluster of excellence 'Origin and Structure of the Universe' and support by the European Commission under the Marie Curie Intra-European Fellowship Programme in FP7. SK and ANG acknowledge support by DFG grant Kl 766/16-1. CT and JGo acknowledge support by the Spanish Ministry of Science and Innovation under project grants AYA2009-14000-C03-01, AYA2010-21887-C04-01 ('Estallidos') and AYA2011-24780/ESP (including Feder funds). SCa, SCo, GT and SP acknowledge support from ASI grant I/011/07/0.

REFERENCES

Andersen M. I. et al., 2000, A&A, 364, L54

Asplund M., Grevesse N., Sauval A. J., 2005, in Barnes, III, T. G., Bash F. N., eds, ASP Conference Series, Vol. 336, Cosmic Abundances as Records of Stellar Evolution and Nucleosynthesis. Astron. Soc. Pac., San Francisco, p. 25

Asplund M., Grevesse N., Sauval A. J., Scott P., 2009, A&AR, 47, 481
Baumgartner W. H. et al., 2010, GCN Circ., 10434
Becker G. D., Sargent W. L. W., Rauch M., Calverley A. P., 2011, ApJ, 735, 93
Berger E., Penprase B. E., Cenko S. B., Kulkarni S. R., Fox D. B., Steidel C. C., Reddy N. A., 2006, ApJ, 642, 979
Berger E. et al., 2007, ApJ, 665, 102
Bloom J. S., Nugent P. E., 2011, GCN Circ., 10433
Bloom J. S., Kulkarni S. R., Djorgovski S. G., 2002, AJ, 123, 1111
Bohlin R. C., 2007, in Sterken C., ed., ASP Conf. Ser. Vol. 364, The Future of Photometric, Spectrophotometric and Polarimetric Standardization. Astron. Soc. Pac., San Francisco, p. 315
Bohlin R. C., Colina L., Finley D. S., 1995, AJ, 110, 1316
Bromm V., Loeb A., 2002, ApJ, 575, 111
Bromm V., Loeb A., 2006, ApJ, 642, 382
Campana S. et al., 2007, ApJ, 654, L17
Campana S., Thöne C. C., de Ugarte Postigo A., Tagliaferri G., Moretti A., Covino S., 2010, MNRAS, 402, 2429
Cenko S. B., Bloom J. S., Perley D. A., Cobb B. E., 2010a, GCN Circ., 10443
Cenko S. B., Perley D. A., Morgan A. N., Klein C. R., Bloom J. S., Butler N. R., Cobb B. E., 2010b, GCN Circ., 10752
Chary R., Berger E., Cowie L., 2007, ApJ, 671, 272
Chary R., Surace J., Carey S., Berger E., Fazio G., 2009, GCN Circ., 9582
Chornock R., Cucchiara A., Fox D., Berger E., 2010, GCN Circ., 10466
Christensen L., Fynbo J. P. U., Prochaska J. X., Thöne C. C., de Ugarte Postigo A., Jakobsson P., 2011, ApJ, 727, 73
Cucchiara A. et al., 2011, ApJ, 736, 7
D'Avanzo P. et al., 2010, A&A, 522, A20
D'Elia V. et al., 2007, A&A, 467, 629
D'Elia V. et al., 2010, A&A, 523, A36
D'Elia V., Campana S., Covino S., D'Avanzo P., Piranomonte S., Tagliaferri G., 2011, MNRAS, 418, 680
D'Odorico S. et al., 2006, Proc. SPIE, 6269, 626933
De Cia A. et al., 2011, MNRAS, 412, 2229
de Ugarte Postigo A., Thöne C. C., Vergani S. D., Milvang-Jensen B., Fynbo J. P. U., 2010a, GCN Circ., 10445
de Ugarte Postigo A. et al., 2010b, A&A, 513, A42
de Ugarte Postigo A. et al., 2012, A&A, 548, A11
Dessauges-Zavadsky M., Prochaska J. X., D'Odorico S., Calura F., Matteucci F., 2006, A&A, 445, 93
Elíasdóttir Á. et al., 2009, ApJ, 697, 1725
Erb D. K., Shapley A. E., Pettini M., Steidel C. C., Reddy N. A., Adelberger K. L., 2006, ApJ, 644, 813
Evans P. A. et al., 2009, MNRAS, 397, 1177
Förster-Schreiber N. M. et al., 2009, ApJ, 706, 1364
Fruchter A. S. et al., 2006, Nat, 441, 463
Fynbo J. P. U. et al., 2006, A&A, 451, L47
Fynbo J. P. U., Prochaska J. X., Sommer-Larsen J., Dessauges-Zavadsky M., Møller P., 2008, ApJ, 683, 321
Fynbo J. P. U. et al., 2009, ApJS, 185, 526
Gall C., Hjorth J., Andersen A. C., 2011, A&AR, 19, 43
Gehrels N. et al., 2004, ApJ, 611, 1005
Goldoni P., Royer F., François P., Horrobin M., Blanc G., Vernet J., Modigliani A., Larsen J., 2006, Proc. SPIE, 6269, 62692K
Gorosabel J., Lund N., Brandt S., Westergaard N. J., Castro Cerón J. M., 2004, A&A, 427, 87
Greiner J. et al., 2008, PASP, 120, 405
Greiner J. et al., 2009a, ApJ, 693, 1610
Greiner J. et al., 2009b, ApJ, 693, 1912
Greiner J. et al., 2009c, A&A, 498, 89
Greiner J. et al., 2011, A&A, 526, A30
Grevesse N., Sauval A. J., 1998, Space Sci. Rev., 85, 161
Groot P. et al., 2010, GCN Circ., 10441
Guimarães R., Petitjean P., de Carvalho R. R., Djorgovski S. G., Noterdaeme P., Castro S., Poppe P. C. D. R., Aghaee A., 2009, A&A, 508, 133
Han X. H., Hammer F., Liang Y. C., Flores H., Rodrigues M., Hou J. L., Wei J. Y., 2010, A&A, 514, A24
Jakobsson P. et al., 2006, A&A, 447, 897
Jakobsson P., Malesani D., Villforth C., Hjorth J., Watson D. J., Tanvir N. R., 2010, GCN Circ., 10438
Jenkins E. B., 2009, ApJ, 700, 1299
Jiang L., Fan X., Vestergaard M., Kurk J. D., Walter F., Kelly B. C., Strauss M. A., 2007, AJ, 134, 1150
Kalberla P. M. W., Burton W. B., Hartmann D., Arnal E. M., Bajaja E., Morras R., Pöppel, W. G. L., 2005, A&A, 440, 775
Kann D. A., Masetti N., Klose S., 2007, AJ, 133, 1187
Kann D. A. et al., 2010, ApJ, 720, 1513
Kawai N. et al., 2006, Nat, 440, 184
Kelson D. D., 2003, PASP, 115, 688
Kewley L. J., Ellison S. L., 2008, ApJ, 681, 1183
Kissler-Patig M. et al., 2008, A&A, 491, 941
Kistler M. D., Yüksel H., Beacom J. F., Hopkins A. M., Wyithe J. S. B., 2009, ApJ, 705, L104
Kocevski D., West A. A., 2011, ApJ, 735, L8
Krühler T. et al., 2008, ApJ, 685, 376
Krühler T., Nicuesa Guelbenzu A., Klose S., Greiner J., Afonso P., 2010, GCN Circ., 10439
Krühler T. et al., 2011a, A&A, 526, A153
Krühler T. et al., 2011b, A&A, 534, A108
Law D. R., Steidel C. C., Erb D. K., Larkin J. E., Pettini M., Shapley A. E., Wright S. A., 2009, ApJ, 697, 2057
Ledoux C., Petitjean P., Fynbo J. P. U., Møller P., Srianand R., 2006, A&A, 457, 71
Ledoux C., Vreeswijk P. M., Smette A., Fox A. J., Petitjean P., Ellison S. L., Fynbo J. P. U., Savaglio S., 2009, A&A, 506, 661
Lehnert M. D., Nesvadba N. P. H., Le Tiran L., Di Matteo P., van Driel W., Douglas L. S., Chemin L., Bournaud F., 2009, ApJ, 699, 1660
Maiolino R. et al., 2008, A&A, 488, 463
Mannucci F. et al., 2009, MNRAS, 398, 1915
Mannucci F., Cresci G., Maiolino R., Marconi A., Gnerucci A., 2010, MNRAS, 408, 2115
Mao J., Malesani D., D'Avanzo P., Covino S., Li S., Jakobsson P., Bai J. M., 2012, A&A, 538, A1
Modigliani A. et al., 2010, Proc. SPIE, pp. 773728–773728–12
Patel M., Warren S. J., Mortlock D. J., Fynbo J. P. U., 2010, A&A, 512, L3
Peng C. Y., Ho L. C., Impey C. D., Rix H.-W., 2002, AJ, 124, 266
Perley D. A. et al., 2010, MNRAS, 406, 2473
Pettini M., Ellison S. L., Bergeron J., Petitjean P., 2002, A&A, 391, 21
Piranomonte S. et al., 2008, A&A, 492, 775
Price P. A. et al., 2007, ApJ, 663, L57
Prochaska J. X., Gawiser E., Wolfe A. M., Castro S., Djorgovski S. G., 2003, ApJ, 595, L9
Prochaska J. X., Herbert-Fort S., Wolfe A. M., 2005, ApJ, 635, 123
Prochaska J. X., Chen H.-W., Bloom J. S., 2006, ApJ, 648, 95
Prochaska J. X., Chen H.-W., Dessauges-Zavadsky M., Bloom J. S., 2007, ApJ, 666, 267
Prochaska J. X., Chen H.-W., Wolfe A. M., Dessauges-Zavadsky M., Bloom J. S., 2008, ApJ, 672, 59
Prochaska J. X. et al., 2009, ApJ, 691, L27
Prochter G. E. et al., 2006, ApJ, 648, L93
Puech M., Hammer F., Flores H., Östlin G., Marquart T., 2006, A&A, 455, 119
Puech M., Hammer F., Lehnert M. D., Flores H., 2007, A&A, 466, 83
Rafelski M., Wolfe A. M., Prochaska J. X., Neeleman M., Mendez A. J., 2012, ApJ, 755, 89
Rau A. et al., 2010, ApJ, 720, 862
Robertson B., Bullock J. S., Cox T. J., Di Matteo T., Hernquist L., Springel V., Yoshida N., 2006, ApJ, 645, 986
Rowlinson A., 2010, GCN Circ., 10444
Rowlinson A. et al., 2010, GCN Circ., 10430
Ruiz-Velasco A. E. et al., 2007, ApJ, 669, 1
Salvaterra R., Campana S., Chincarini G., Tagliaferri G., Covino S., 2007, MNRAS, 380, L45
Salvaterra R. et al., 2009, Nat, 461, 1258
Salvaterra R., Ferrara A., Dayal P., 2011, MNRAS, 414, 847

Sari R., Piran T., Narayan R., 1998, ApJ, 497, L17
Savage B. D., Sembach K. R., 1996, A&AR, 34, 279
Savaglio S., 2006, New J. Phys., 8, 195
Savaglio S., Panagia N., Stiavelli M., 2000, in Franco J., Terlevich L., López-Cruz O., Aretxaga I., eds, ASP Conference Proceedings, Vol. 215, Cosmic Evolution and Galaxy Formation: Structure, Interactions, and Feedback. p. 65
Savaglio S. et al., 2005, ApJ, 635, 260
Savaglio S., Glazebrook K., LeBorgne D., 2009, ApJ, 691, 182
Schady P., Savaglio S., Krühler T., Greiner J., Rau A., 2011, A&A, 525, A113
Schlegel D. J., Finkbeiner D. P., Davis M., 1998, ApJ, 500, 525
Skrutskie M. F. et al., 2006, AJ, 131, 1163
Skúladóttir A., 2010, Master Thesis, Univ. of Copenhagen (http://dark.nbi.ku.dk/calendar/calendar2010/asa_defense/AsaSkuladottir.pdf/)
Sparre M. et al., 2011, ApJ, 735, L24
Springel V., 2005, MNRAS, 364, 1105
Stratta G., Maiolino R., Fiore F., D'Elia V., 2007, ApJ, 661, L9
Stratta G., Gallerani S., Maiolino R., 2011, A&A, 532, A45
Sudilovsky V., Savaglio S., Vreeswijk P., Ledoux C., Smette A., Greiner J., 2007, ApJ, 669, 741
Swinbank A. M., Bower R. G., Smith G. P., Wilman R. J., Smail I., Ellis R. S., Morris S. L., Kneib J.-P., 2009, MNRAS, 376, 479
Tanvir N. R. et al., 2009, Nat, 461, 1254
Thöne C. C., Greiner J., Savaglio S., Jehin E., 2007, ApJ, 671, 628
Thöne C. C. et al., 2008, A&A, 489, 37
Thöne C. C. et al., 2011, MNRAS, 414, 479
Totani T., Kawai N., Kosugi G., Aoki K., Yamada T., Iye M., Ohta K., Hattori T., 2006, PASJ, 58, 485
Tremonti C. A. et al., 2004, ApJ, 613, 898
van Dokkum P. G., 2001, PASP, 113, 1420
Vergani S. D., Petitjean P., Ledoux C., Vreeswijk P. M., Smette A., Meurs E. J. A., 2009, A&A, 503, 771
Vernet J. et al., 2011, A&A, 536, A105
Vreeswijk P. M. et al., 2004, A&A, 419, 927
Vreeswijk P. M. et al., 2006, A&A, 447, 145
Vreeswijk P. M. et al., 2007, A&A, 468, 83
Watson D., Jakobsson P., 2012, ApJ, 754, 89
Watson D. et al., 2006, ApJ, 652, 1011
Watson D., Hjorth, J., Fynbo, J. P. U., Jakobsson, P., Foley, S., Sollerman, J., Wijers, R. A. M. J., 2007, ApJ, 660, L101
Wiersema K. et al., 2011, GCN Circ., 12431
Wolfe A. M., Gawiser E., Prochaska J. X., 2005, A&AR, 43, 861
Woosley S. E., Bloom J. S., 2006, A&AR, 44, 507
Woosley S. E., Heger A., 2006, ApJ, 637, 914
Yüksel H., Kistler M. D., Beacom J. F., Hopkins A. M., 2008, ApJ, 683, L5
Zafar T., Watson D. J., Malesani D., Vreeswijk P. M., Fynbo J. P. U., Hjorth J., Levan A. J., Michałowski M. J., 2010, A&A, 515, A94
Zafar T., Watson D., Fynbo J. P. U., Malesani D., Jakobsson P., de Ugarte Postigo A., 2011, A&A, 532, A143

This paper has been typeset from a TEX/LATEX file prepared by the author.